

Ultrawide-Band/High-Frequency Photodetectors

Kazutoshi Kato, *Member, IEEE*

(Invited Paper)

Abstract—The two main trends in the progress of ultrawide-band/high-frequency photodetectors (PD's), improving the bandwidth-efficiency product and obtaining a high saturation current, are reviewed. With respect to achieving large bandwidth-efficiency, the limiting factors and potentials of edge-coupled (waveguide, waveguide-fed, traveling-wave, periodic-traveling-wave), resonant-cavity, and refracting-facet photodiodes, as well as the avalanche photodiode are discussed. Regarding high-saturation current, the author estimated how much the space-charge effect limits the saturation current and two ways to reduce the space-charge effect are outlined. One way is to distribute the photocarriers along the edge-coupled PD's and the other is to increase the carrier velocity using a uni-traveling carrier structure. The waveguide-photodiode-based technologies that we have developed are also presented; namely the design and fabrication of a 100-GHz waveguide photodiode (WGPd), uni-traveling carrier WGPd, 60-GHz packaging, and a 20-GHz large-core WGPd for the planar lightwave circuit integration. A 50-Gb/s receiver opto-electronic integrated circuit technology based on the WGPd is also presented.

Index Terms—Avalanche photodiodes, opto-electronics integrated circuits, photodetectors, photodiodes, refracting-facet photodiodes, resonant-cavity-enhanced photodetectors, traveling-wave photodetectors, uni-traveling-carrier photodiodes, waveguide photodetectors.

I. INTRODUCTION

THE photodetector (PD) is a key component in optical transmission and optical measurement systems. The basic requirement for the PD is high efficiency, and this requirement becomes especially important as systems become faster. Optical-fiber communication systems with a data rate of 40 Gb/s per channel have been demonstrated, and much effort has been focused on increasing the efficiency of PD's for systems operating at this and higher data rates. Among several technologies for overcoming the theoretical bandwidth-efficiency limit of conventional vertically illuminated photodetectors (VPD's), the edge-coupled PD has shown good potential from an early stage. Recently, this technology has been applied in some measurement systems with a bandwidth of over 100 GHz [1].

The development of the optical-fiber amplifier has created a new demand for high available-power PD's. Some novel systems use a fiber amplifier as a preamplifier in the receiver, which relieves or even eliminates the burden imposed on the electrical preamplifier. In such systems, a highly amplified

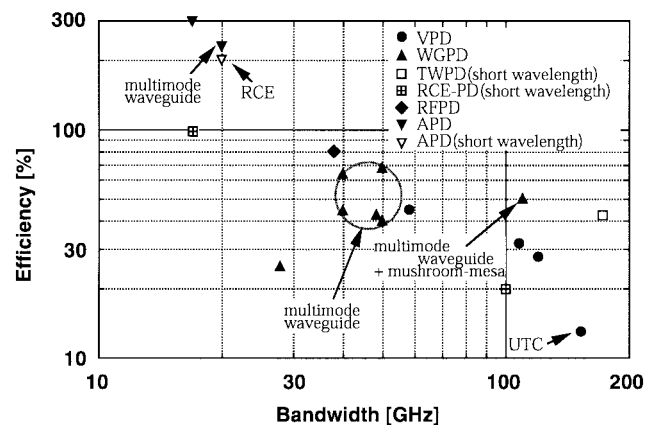


Fig. 1. Performances of the reported PD's: VPD, WGPd, TWPD, RCE-PD, RFPD, and APD.

input light is introduced into the PD. This means that the maximum available input power or output current has to be more than two orders of magnitude higher than that in conventional systems. Improving the saturation current is, therefore, important for such systems, especially for a long wavelength at which an optical-fiber amplifier provides a gain. The fiber-optic links for millimeter-wave (30–90 GHz) radio communication systems [2], [3] are typical analog applications and the 40-Gb/s directly driven decision circuit [4] is a new digital application.

Thus, the two major trends in PD development are a large bandwidth-efficiency product and a high saturation current. This paper first outlines these trends and their limiting factors. It then discusses several PD technologies based on the waveguide photodiode (WGPd) for these two trends. Finally, it presents a recently developed WGPd-based receiver opto-electronic integrated circuit (OEIC).

II. PD'S FOR LARGE BANDWIDTH-EFFICIENCY PRODUCT

A large bandwidth-efficiency product is an essential factor for bringing out the full potential of a receiver. Especially at frequencies beyond 20 GHz, higher efficiency helps relieve the burden imposed on electrical components and also makes their integration easier. Several structures have been investigated as ways to overcome the bandwidth-efficiency limit of the conventional VPD. Fig. 1 shows the reported bandwidth-efficiency performance of PD's with various structures. In this section, we discuss the bandwidth-efficiency tradeoff for each of these PD's and see which ones meet a certain requirement.

Manuscript received October 12, 1998; revised March 24, 1999.

The author is with NTT Photonics Laboratories, Atsugi, Kanagawa 243-0198, Japan (e-mail: kkato@aecl.ntt.co.jp).

Publisher Item Identifier S 0018-9480(99)05196-0.

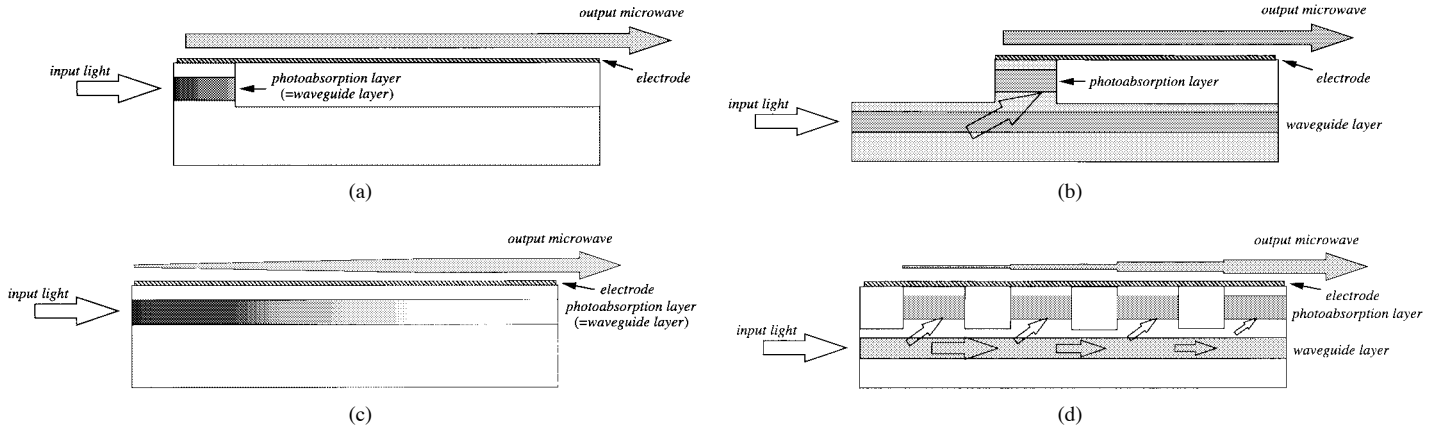


Fig. 2. Device structures. (a) WGPd. (b) WG-fed-PD. (c) TWPD. (d) P-TWPD.

A. Bandwidth-Efficiency Tradeoff

PD's have a photoabsorption layer that converts input light into carriers such as electrons and holes. For a ultrawide-band response, the carrier-transit time in the photoabsorption layer should be much shorter than the required system response. The 3-dB-down electrical bandwidth f_t limited by the carrier-transit time is related to the carrier-transit distance D [5] such that

$$f_t \cong \frac{3.5\bar{v}}{2\pi D} \quad (1)$$

$$\frac{1}{\bar{v}^4} = \frac{1}{2} \left(\frac{1}{v_e^4} + \frac{1}{v_h^4} \right) \quad (2)$$

where v_e and v_h are the electron and hole saturation velocities, respectively. Using $v = 5.3 \times 10^6$ cm/s for an InGaAs (for 1.3–1.6 μm : long wavelength) or GaAs (for 0.85 μm : short wavelength) photoabsorption layer, D of less than 0.3 and 0.1 μm are, respectively, required for 100- and 300-GHz bandwidths.

Here, we estimate the upper limit of the bandwidth-efficiency product of conventional VPD's. The p-i-n, Schottky, or metal-semiconductor-metal (MSM) structure can be applied to the VPD. First, we discuss the p-i-n or Schottky VPD. The common technique for improving the internal quantum efficiency of a VPD is a double-pass scheme using return light reflected by the electrode. This technique is easily applied to transparent InP substrate (for long wavelength), while an additional process, such as substrate removal, is required for absorbent GaAs substrate (for short wavelength). Since the input light travels vertically in the photoabsorption layer, the internal quantum efficiency is expressed as

$$\begin{aligned} \eta_{\text{int}} &= (1 + re^{-\alpha d})(1 - e^{-\alpha d}) \\ &\cong (1 + r)\alpha d \end{aligned} \quad (3)$$

where r , α , and d are the reflection coefficient at the electrode, absorption coefficient, and thickness of the photoabsorption layer, respectively. The above approximation is suited for high-speed PD's with small d . From (1) and (2), in which $D = d$ in the VPD, the bandwidth-efficiency limit is

$$f_t \cdot \eta_{\text{int}} \cong \frac{3.5\bar{v}(1+r)\alpha}{2\pi}. \quad (4)$$

In the case of $r = 0$ –1, the bandwidth-efficiency products are 20–40 and 34–68 GHz at 1.55 and 1.3 μm for InGaAs when the InGaAs absorption coefficients are $0.68 \mu\text{m}^{-1}$ at 1.55 μm and $1.16 \mu\text{m}^{-1}$ at 1.3 μm [6], and 30–60 GHz at 0.85 μm for GaAs when the GaAs absorption coefficient is $1.0 \mu\text{m}^{-1}$ [7].

For the metal-semiconductor-metal photodetector (MSM-PD), carrier-transit distance D is roughly approximated as $D \cong \sqrt{d^2 + W_g^2}$, where W_g is the gap distance. Since its efficiency is also estimated by (3), there is a tradeoff between bandwidth and efficiency similar to that with p-i-n or Schottky types.

In a real photodiode, other factors, such as the capacitance resistance (CR) time constant, and optical coupling loss, degrade performance. The circles in Fig. 1 show the performance of reported VPD's aiming at a large bandwidth-efficiency product [8]–[11]. The possible bandwidth-efficiency product ranges from 20 to 35 GHz.

B. WGPd

The edge-coupled WGPd [Fig. 2(a)] has been widely investigated as one candidate for overcoming the bandwidth-efficiency tradeoff in the VPD. The WGPd, as its name implies, has an optical waveguide structure in itself. This structure permits the bandwidth and efficiency to be specified almost independently because the internal efficiency is determined not by the photoabsorption layer thickness d , but by the waveguide length. In 1986, the first high-speed edge-coupled WGPd was demonstrated. It had a bandwidth of 28 GHz and an efficiency of 25% [12].

The chief drawback of edge-coupled PD's is that it is difficult to obtain efficient optical coupling or a good overlap integral between the input optical field and the optical field at the PD. This is because the diameter of an input light, even when focused by lenses, is no less than 2 μm , while the optical field distribution at the PD with a thin photoabsorption layer is narrower than 1 μm .

One way to avoid the coupling problem is to enlarge the optical field distribution at the PD without increasing the thickness of the photoabsorption layer. To achieve this, double-core multimode waveguide structures were proposed in 1991 [13], [14] (see Section IV). The double-core consists of transparent

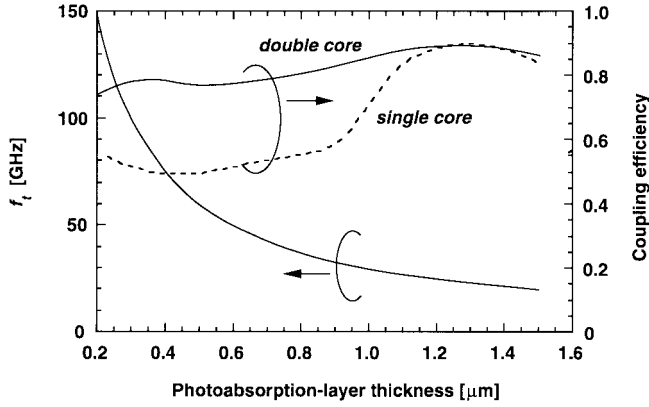


Fig. 3. Calculated carrier-transit-time-limiting bandwidth and coupling efficiencies.

doped intermediate bandgap layers are set above and/or below the photoabsorption layer. Optically, widely distributed higher order fields appear and they are guided between two cladding layers. Electrically photogenerated carrier transport and electrostatic properties are almost unchanged because the intrinsic layer is still only the photoabsorption layer. The calculated external quantum efficiency of a InP/InGaAsP ($\lambda_g = 1.3 \mu\text{m}$)/InGaAs/InGaAsP ($\lambda_g = 1.3 \mu\text{m}$)/InP double-core WGPDP when the double-core thickness is constant at $1.8 \mu\text{m}$ is shown in Fig. 3 along with that of a conventional single-core WGPDP for comparison. Here, it is assumed that the input light has a $1.3\text{-}\mu\text{m}$ spot-size (halfwidth of $1/e$ maximum field), which is typical for input light focused by a double-lens system. These structures are designed to detect a $1.55\text{-}\mu\text{m}$ wavelength. The calculated coupling efficiency of the double-core structure stays at more than about 80% with varying photoabsorption layer thickness. That of the conventional one, however, is lower than 60% at around $0.2\text{--}1.0 \mu\text{m}$, which unfortunately is just the thickness for $30\text{--}150\text{-GHz}$ bandwidth. Owing to the high coupling efficiency, the double-core multimode waveguide structure became popular for the WGPDP. The triangles circled in the middle of Fig. 1 are for WGPDP's employing the double-core multimode waveguide structure [14]–[18]. These WGPDP's have a bandwidth-efficiency product of around 20 GHz, and one can see that this was the first breakthrough for the WGPDP.

What then limits the bandwidth-efficiency product at these WGPDP's? Since electrically the WGPDP is a lumped-element device, the CR time constant is another limiting factor and its total bandwidth $f_{3\text{dB}}$ is expressed by

$$f_{3\text{dB}} = \frac{f_t}{\sqrt{1 + \left(\frac{f_t}{f_{\text{CR}}}\right)^2}} = \frac{f_{\text{CR}}}{\sqrt{1 + \left(\frac{f_{\text{CR}}}{f_t}\right)^2}} \quad (5)$$

$$f_{\text{CR}} = \frac{1}{2\pi C(R_s + R_L)} \quad (6)$$

where C is the capacitance of the PD, and R_s and R_L are the parasitic and load resistances. This equation means that $f_{3\text{dB}}$ is decreased by $1/\sqrt{2}$ when f_{CR} is comparable to f_t and, furthermore, that $f_{3\text{dB}}$ is dominated by f_{CR} when f_{CR} is smaller than f_t . Since R_L is 50Ω in practical systems, C must

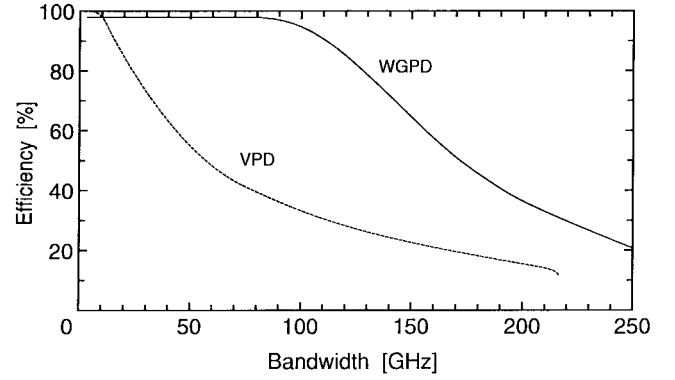


Fig. 4. Calculated performances of WGPDP and VPD.

be decreased. Thus, in previous works, the aim was to decrease the area of the WGPDP's for the $40\text{--}50\text{-GHz}$ bandwidth. In WGPDP's with a small waveguide area of less than $50 \mu\text{m}^2$, R_s , the contact resistance at the top of the waveguide and the lateral resistance at the lower cladding layer, became high and the tradeoff between C and R_s became another problem in enlarging $f_{3\text{dB}}$. This tradeoff becomes more serious when we seek a larger $f_{3\text{dB}}$ because larger f_t needs a thinner photoabsorption layer, which also increases C . A 100-GHz bandwidth, for example, requires a core thickness of less than $0.3 \mu\text{m}$, which results in a capacitance of about 30 fF for a WGPDP of typical size ($50 \mu\text{m}^2$). Since the contact resistance in such a small WGPDP is about 40Ω (which is enhanced by high resistivity at the waveguide-mesa fringe), the total resistance for a $50\text{-}\Omega$ system is 90Ω and the f_{CR} is limited to 60 GHz [17].

To overcome this parasitic tradeoff, a mushroom-mesa waveguide structure was proposed in 1994 (see Section IV) [19]. In this structure, the cladding and intermediate-bandgap layers are wider than the core layer. Thus, one can expect a negligibly small parasitic resistance compared with the $50\text{-}\Omega$ load. Fig. 4 shows the calculated performance of a $1.55\text{-}\mu\text{m}$ WGPDP with a combination of the mushroom-mesa and double-core multimode waveguide configurations along with that of the VPD for comparison [19]. The CR time was also considered in the calculation. In the WGPDP, there is no efficiency degradation at a bandwidth of up to 100 GHz and, above 100 GHz , the bandwidth-efficiency product is $70\text{--}90 \text{ GHz}$ due to the tradeoff between the capacitance and the internal efficiency.

At long wavelength, a $1.5\text{-}\mu\text{m}$ -wide $10\text{-}\mu\text{m}$ -long WGPDP reached 110-GHz bandwidth and 50% efficiency (55-GHz bandwidth-efficiency product) resulting from a capacitance of 15 fF and a resistance of less than 10Ω [20]. In Fig. 1, one can see that the mushroom mesa was the second breakthrough for large-bandwidth WGPDP's. The mushroom mesa can be common technology for not only other edge-coupled photodiodes, such as the traveling-wave PD and waveguide-fed photodiode described below, but also the VPD and refracting-facet photodiode (RFPD). In fact, a VPD employing a similar structure provide the bandwidth of 120 GHz [10].

For a larger bandwidth, the challenge is how to increase $\Gamma\alpha$ (Γ : optical confinement factor, α : photoabsorption coefficient),

which is essential for lumped-element devices. For a large α , the use of the exciton absorption in a multiquantum well (MQW) photoabsorption layer would be effective.

C. Waveguide-Fed Photodiode

Another way to avoid the coupling problem of the edge-coupled photodiode is to use a waveguide-fed photodiode (WG-fed-PD). In this structure, the waveguide is separated from the photoabsorption layer, as shown in Fig. 2(b). It acts as an input waveguide and could be designed to make better coupling with an input light using either a large-field or tapered waveguide [21], [22]. This scheme had originally been investigated as an application for photonic integrated circuits such as coherent lightwave receivers [23] and, from the 1970's to the beginning of the 1990's, many butt-coupling and evanescent-coupling schemes were reported. In the 1990's, though progress in Erbium-doped optical fiber amplifiers (EDFA's) attenuated the necessity of coherent detection, efforts to enlarge the bandwidth using the WG-fed-PD continued, and a butt-coupling type reached 22 GHz [24] while an evanescent-coupling type reached 70 GHz [25] at a 1.55- μm wavelength. The evanescent types achieved 90% internal efficiency even with a 20- μm -long photodiode using a quaternary optical matching layer. Though the bandwidth-efficiency product of these devices has still only reached around 20 GHz because of the coupling loss at the input facet of the waveguide, they have the potential to provide a bandwidth-efficiency product similar to that of the WGP. Though the reported large-bandwidth devices were based on a p-i-n structure, a MSM-type WG-fed-PD could also provide a large bandwidth. Thus far, however, investigations of the MSM-type have focused on a traveling-wave PD, which is discussed below.

D. Distributed PD's

The distributed PD was first proposed in 1990 as a "traveling-wave photodetector," in which photoabsorption occurs in a distributed fashion along the length of a transmission-line structure [26]. The traveling-wave PD has been studied by way of both hybrid [27] and monolithic approaches. Here, we discuss the monolithic types because they have been reported to reach a higher speed. The optical structure of the monolithic traveling-wave PD is similar to the WGP or WG-fed-PD, but its electrically distributed structure can overcome the CR bandwidth limitation of these lumped-element devices. In one possible configuration, the light is guided along the photoabsorptive optical waveguide, as in the WGP, which is concomitant with the transmission line [Fig. 2(c)]. In another configuration, the light is absorbed by a set of photodiodes distributed along a transparent optical waveguide and a transmission line [Fig. 2(d)]. Though these two schemes seem similar, their electrical wave properties are very different; the electrical wave in the former is one-third as fast as the optical wave [28], while that in the latter is about 35% faster than the optical wave [29]. Today, the former type is normally called a traveling-wave photodetector (TWP) and the latter a periodic TWP [30], or velocity-matched

distributed photodetector (VMDP) [29]. In this paper, for convenience, the terms TWP and periodic TWP (P-TWP) are used.

In the TWP and P-TWP, besides the carrier-transit time, the velocity mismatch between the optical and electrical waves limits the bandwidth. The overall bandwidth $f_{3\text{dB}}$ can then be described as

$$f_{3\text{dB}} = \frac{f_t}{\sqrt{1 + \left(\frac{f_t}{f_{\text{VM}}}\right)^2}} \quad (7)$$

where f_{VM} is the bandwidth limited by the velocity mismatch. The velocity mismatch occurs first because the electrical wave travels along the transmission line slower (faster) in the TWP (the P-TWP) than the optical wave in the semiconductor layer. Furthermore, the backward-traveling electrical wave, which turns back at the input end, overlaps the forward-traveling wave in an out-of-phase manner and becomes the second factor inducing the velocity mismatch.

The properties of the p-i-n TWP have been theoretically investigated in detail [30]. The electrical phase velocity V_e and characteristic impedance Z_0 are approximated as

$$V_e = \frac{1}{\sqrt{L_u C_u}} \quad (8)$$

$$Z_0 = \sqrt{\frac{L_u}{C_u}} \quad (9)$$

where L_u and C_u are the inductance and capacitance per unit length of the transmission line, respectively. Since C_u is the capacitance of undoped photoabsorption layer

$$C_u = \epsilon_0 \epsilon_r \frac{w}{d} \quad (10)$$

where ϵ_0 and ϵ_r are the permittivity in a vacuum and the dielectric constant, and w and d are the width and thickness of the photoabsorption layer.

Based on the previous considerations, first we discuss the optical/electrical velocity mismatch. From (8) to (10), one can deduce the relationship among V_e , d , and w as

$$V_e = \frac{d}{\epsilon_0 \epsilon_r w Z_0}. \quad (11)$$

In the case of $Z_0 = 50 \Omega$, the above relationship is plotted with w as a parameter together with the calculated f_t by (1) in Fig. 5. The efficiencies in brackets in Fig. 5 are the calculated coupling efficiencies for the photodiode and input light with a 1.3- μm spot-size. Here, we assume the coupling efficiency in the vertical direction of 80% due to a double-core multimode configuration. One can see that the coupling efficiency decreases with decreasing w because of the horizontal coupling loss. Using these results, one can design the TWP as follows. First, if the target bandwidth is $f_{3\text{dB}} = 100 \text{ GHz}$, the f_t is set at 150 GHz with a certain margin. Next, for $f_t = 150 \text{ GHz}$, d is chosen to be 0.2 μm . Then, possible combinations are $w = 1 \mu\text{m}$ and $V_e = 5.2 \times 10^9 \text{ cm/s}$ or $w = 2 \mu\text{m}$ and $V_e = 2.6 \times 10^9 \text{ cm/s}$. Finally, one can expect optical coupling efficiencies of 45% and 70% with $w = 1 \mu\text{m}$ and $w = 2 \mu\text{m}$, respectively. As one may notice, the practical device width of

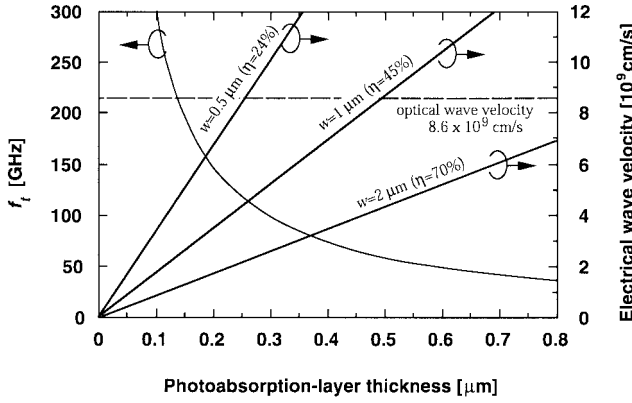


Fig. 5. Calculated carrier-transit-time-limiting bandwidth and electrical wave velocities of the TWPD.

a few microns produces V_e that is much lower than the optical velocity (about 8.6×10^9 cm/s [29]). This is why the TWPD has a slow-wave property in itself and the optical/electrical velocity mismatch is the main factor limiting the bandwidth.

Next, we discuss the bandwidth limited by the velocity mismatch. Distributed PD's have two possible schemes: one has an open load and the other has matched termination at the optical input end. In the open-loaded TWPD, the backward wave is reflected at the input end and overlaps the forward wave, causing forward/backward-wave mismatch. On the other hand, in the terminated TWPD, though the obstructive backward wave is absorbed by the termination, the photocurrent or the internal efficiency is cut by half. In [30], it was concluded that the f_{VM} of the TWPD can be expressed as

$$f_{VM} \cong \frac{\Gamma \alpha V_e}{2\pi \left(1 - \frac{V_e}{V_o}\right)} \quad (\text{with matched termination}) \quad (12)$$

$$f_{VM} \cong \frac{\Gamma \alpha V_e}{3\pi} \quad (\text{with open load}) \quad (13)$$

where Γ and V_o are the optical waveguide confinement factor and optical wave velocity, respectively.

Based on the above results, we estimate the bandwidth-efficiency product. Since V_e/V_o is about 0.3 ($w = 2 \mu\text{m}$) – 0.6 ($w = 1 \mu\text{m}$), (12) indicates that the terminated TWPD has a bandwidth about two to four times as large as that of the open-loaded TWPD. Considering these bandwidths together with the fact that the efficiency is cut by half at the terminated TWPD, as well as the coupling efficiencies of 70% ($w = 2 \mu\text{m}$) – 45% ($w = 1 \mu\text{m}$), we find that these two TWPD's have a similar bandwidth-efficiency product. Furthermore, as described in [30], (13) indicates that the light is absorbed in the effective photoabsorption length of $1.5/\Gamma\alpha$ and the f_{VM} would be identical to the WGPD with the same effective length even if the TWPD is much longer than the WGPD. Thus, assuming the TWPD and WGPD are designed to have the same bandwidth, the TWPD could have 100% internal efficiency with its long waveguide scheme, while the WGPD could have 78% internal efficiency. Consequently, the bandwidth-efficiency product of

the open-loaded and terminated TWPD's would be greater than that of the WGPD by a factor 1.3 ($=0.78^{-1}$).

At a short wavelength of $0.83 \mu\text{m}$, a $1\text{-}\mu\text{m}$ -wide $7\text{-}\mu\text{m}$ -long TWPD based on a GaAs p-i-n photodiode achieved a 172-GHz bandwidth and 42% efficiency [31]. The performance is plotted by squares in Fig. 1. At a long wavelength, a 1-mm-long TWPD based on InGaAs Schottky photodiode showed a 40-GHz bandwidth [32], which testifies to the independence of the bandwidth from the device length as predicted above.

The challenge in increasing the bandwidth of the TWPD is how to increase $\Gamma\alpha$ as well as improve the coupling efficiency. The policy of large $\Gamma\alpha$ is identical to that for WGPD's and contradicts that for achieving higher saturation current. To improve the coupling efficiency, the double-core multimode structure can be applied to the TWPD because the velocity mismatch between each optical mode is negligible at the inherently short effective photoabsorption length of the TWPD.

The concept of the P-TWPD was first realized in a photonic-to-microwave transformer [33]. A P-TWPD consists of an array of individual photodiodes serially connected by a rather long passive optical waveguide and transmission line. Since the backward electrical wave seriously disturbs the forward wave along the long transmission line, the termination at the optical input end, which results in the cutting of the efficiency by half, should be employed for operation as a P-TWPD. The electrical wave velocity in the transmission line on semiconductor substrate is about 35% faster than that of the optical wave [29], while the situation is the opposite in the TWPD. The great advantage of the P-TWPD is its ability to perform optical/electrical-wave matching using an electrical delay line [33] or an electrical slow-wave line, and when the velocity matching is performed, this PD is called a VMDP [29]. The slow-wave line has been intensively investigated for micro-wave/millimeter-wave circuits and is known to be achieved by periodic capacitance loading, which can be realized by the capacitance of the periodically arrayed individual photodiode at the P-TWPD [29].

Two expressions of the bandwidth of the P-TWPD have been presented [29], [30]. Both predict an infinite f_{VM} when velocity matching is performed. Thus, considering (7), the total bandwidth of the P-TWPD is limited by the carrier-transit time of the individual photodiode. In addition, in reality, optical/electrical wave mismatch should occur inside each few microns-long photodiode so as to provide a lumped-element property just like that in the TWPD. Thus, the frequency response of the P-TWPD is expected to be similar to that of a short (few microns long) TWPD with termination. The advantage of the P-TWPD is that the efficiency is increased to nearly 50% and the saturation current can be increased without degrading the bandwidth. Though parasitic factors, such as optical reflections and scattering at each photodiode, depend on the complexity of the structure, one may expect similar values to those of the TWPD and WGPD. A P-TWPD based on the GaAs-MSM-PD (for a short wavelength) has reached around 50 GHz [29] (the efficiency was not discussed). One based on the InGaAs-MSM-PD (for a long wavelength) has reached 78 GHz [34] (the efficiency was 7.5%).

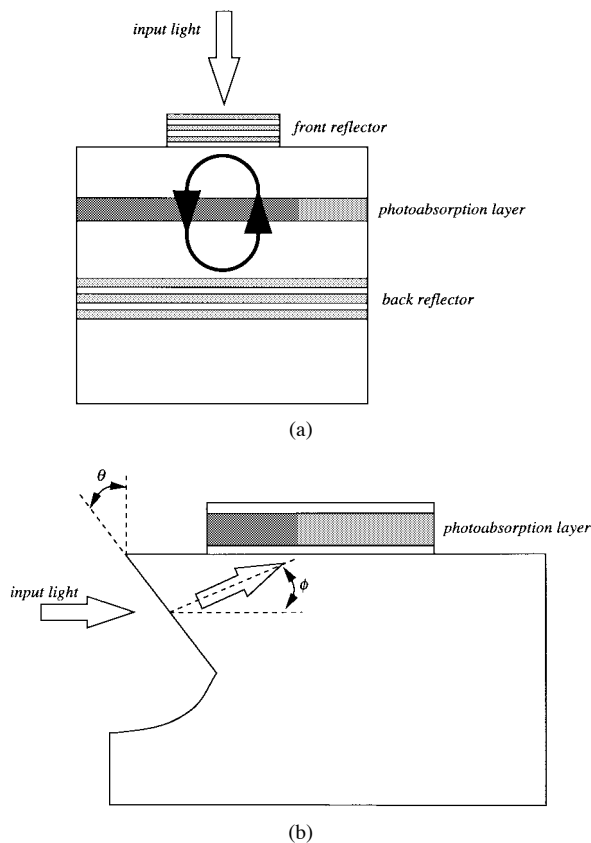


Fig. 6. Device structures. (a) RCE-PD. (b) RFPD.

E. Other PD's

Another approach to overcoming the bandwidth-efficiency tradeoff in the VPD is to enhance cavity resonance. As shown in Fig. 6(a), the resonant-cavity-enhanced photodetector (RCE-PD) consists of a thin photoabsorption layer sandwiched between two reflectors, and the incoming light interferes constructively with the reflected component from the reflectors, which is similar to what happens in vertical-cavity surface-emitting lasers. A theoretical investigation showed that a back reflector with 0.99 reflectivity would push the efficiency of the VPD to more than 90% (i.e., increased it by a factor four) even when the thickness of the photoabsorption layer is less than $0.1 \mu\text{m}$, which would then result in producing an expected bandwidth-efficiency product about 140 GHz [7]. Another advantage of the RCE-PD is its wavelength selectivity, which makes it useful as a receiver in wavelength division multiplexing (WDM) systems. Several earlier works focused on increasing the efficiency and selectivity rather than on enlarging bandwidth. The resonant-cavity-enhanced (RCE) operation was first demonstrated in 1990 in a short-wavelength Schottky [35], and heterojunction phototransistors [36] using a quarter-wave-stack Bragg reflector as a back reflector. Then, p-i-n, MSM, and avalanche photodiode structures were applied to the RCE configuration at a long or short wavelength [37]. Large bandwidth-efficiency products of 17 GHz ($17 \text{ GHz} \times 99\%$) and 20 GHz ($100 \text{ GHz} \times 20\%$) have been obtained with a short-wavelength GaAs p-i-n [38] and Schottky [39] RCE-PD, respectively, which are shown by \boxplus in Fig. 1.

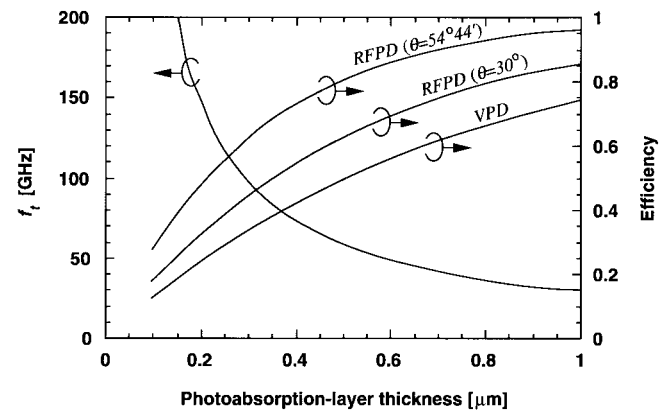


Fig. 7. Calculated carrier-transit-time-limiting bandwidth and efficiencies of RFPD (and VPD as a reference).

Generally, with Bragg reflectors, it is more difficult to realize a high reflectivity for a long wavelength than it is for a short wavelength. This is because the refractive index difference between InP and InGaAs is at least two times smaller than for GaAs/AlAs [37]. To overcome this problem, a GaAs/AlAs reflector was wafer-fused to a long-wavelength InGaAs p-i-n photodiode layer. The results were an efficiency of 94% (enhanced by a factor 16) and a linewidth of 14 nm [40].

When instead of an extremely large bandwidth we need a moderate one of around 30–50 GHz, an effective method for improving the efficiency is to use a RFPD. The RFPD was first demonstrated as a photodiode suitable for low-cost hybrid integration technology in 1996 [41]. In the RFPD, as shown in Fig. 6(b), the incoming light refracts at the angled facet and passes through the photoabsorption layer at angle ϕ . Thus, the effective optical path increases by $1/\sin \phi$, and the internal efficiency becomes higher than that in a VPD with the same epilayer. Fig. 7 shows the calculated internal efficiencies of RFPD's ($\theta = 30^\circ$ and $54^\circ 44'$) and a VPD as well as the carrier-transit-time-limited bandwidth, assuming the use of the double-pass scheme with 100% reflection at the top electrode. When the thickness of the photoabsorption layer is $0.6\text{--}1.0 \mu\text{m}$, which corresponds to a bandwidth of 30–50 GHz, the RFPD with a $54^\circ 44'$ -angled facet provides an efficiency of more than 80%, which is higher than that of the VPD by a factor of 1.5.

The angled facet was obtained by using the feature that a (111)A facet is revealed with an angle of $54^\circ 44'$ in the InP (001) surface by anisotropic chemical etching. A packaged RFPD with a $1.0\text{-}\mu\text{m}$ -thick InGaAs photoabsorption layer showed a bandwidth of 38 GHz (somewhat larger than the calculated result due to the peaking effect) and an efficiency of 80% (1 A/W) at a $1.55\text{-}\mu\text{m}$ wavelength [42]. This RFPD is signified as a diamond in Fig. 1.

Another advantage of the RFPD is that it has a larger vertical misalignment tolerance to input light than edge-coupled PD's do. This is because the vertical shift of the beam position at the facet corresponds to a horizontal shift after refraction. Thus, for an RFPD designed for 30–50 GHz, a certain misalignment tolerance can be obtained by increasing the device length with keeping the margin of the CR limit. This contributes to module

cost reduction by simplifying the optical coupling components [42].

A great number of works have been reported on avalanche photodiodes (APD's) operating in the 10-Gb/s region. A separate absorption and multiplication (SAM) structure has been commonly used to improve the gain-bandwidth product and reduce the multiplication noise [43], [44]. The VPD scheme has been popular for the APD, and a bandwidth of 17 GHz, an efficiency of 74%, and a multiplication factor of four, which results in a bandwidth-efficiency product of 50 GHz, have been obtained at a long wavelength by a superlattice SAM-APD with a 0.8- μm -thick photoabsorption layer [45]. (This device was designed for operation at 10 Gb/s and the largest gain-bandwidth product, 110 GHz, was observed at around that frequency.) A larger bandwidth would require a thinner photoabsorption layer, but this would reduce the efficiency because of the same tradeoff found in the VPD.

Using the same technique described earlier, an edge-coupled WSPD structure is expected to overcome this tradeoff. The waveguide superlattice APD was first reported in 1994 [46]. Afterwards, a waveguide superlattice APD with a 0.3- μm -thick photoabsorption layer reached 72%-efficiency (0.9-A/W responsivity) and 3.2-multiplication factor at 20-GHz at 1.55- μm wavelength [47]. This indicates a 47-GHz bandwidth-efficiency product. (This device had the largest gain-bandwidth product, 160 GHz at around 13 GHz.) The performance of the waveguide APD and a vertically illuminated APD is signified by the \blacktriangledown in Fig. 1.

The RCE structure is also expected to enlarge the bandwidth of the APD. A 1991 work [48] on RCE-APD's showed an efficiency of 49% even with a 0.09- μm -thick photoabsorption layer. Recently, a 14- μm -diameter RCE-APD with a 0.035- μm photoabsorption layer achieved a unity gain bandwidth of 23 GHz and a bandwidth-efficiency product of around 40 GHz at 20 GHz at a short wavelength [49]. This is signified by the ∇ in Fig. 1. (This device was designed for operation at 10 Gb/s and the largest gain-bandwidth product, 130 GHz, was observed at around 10 Gb/s.) The bandwidth-limiting factor was thought to be the CR time constant, which implies the possibility of obtaining more bandwidth by reducing the diameter.

III. PD'S FOR A HIGH-SATURATION CURRENT

A. Limiting Factors

One of the factors that limits the maximum available output current is the nonlinearity of the PD response. Nonlinearity causes a harmonic power which degrades the carrier-to-noise ratio in analog systems. High-speed-PD nonlinearity under high-power illumination has been investigated numerically [50]–[54] and experimentally [29], [55]–[61]. These studies indicated that nonlinearity is caused by a decrease in the electric field and then a lowering of the carrier velocity due to a space-charge effect or an electric-field screening effect. The space-charge effect trends to be more serious with wider bandwidth PD's because such PD's generally have a smaller photoabsorption volume of about 1 μm^3 and their

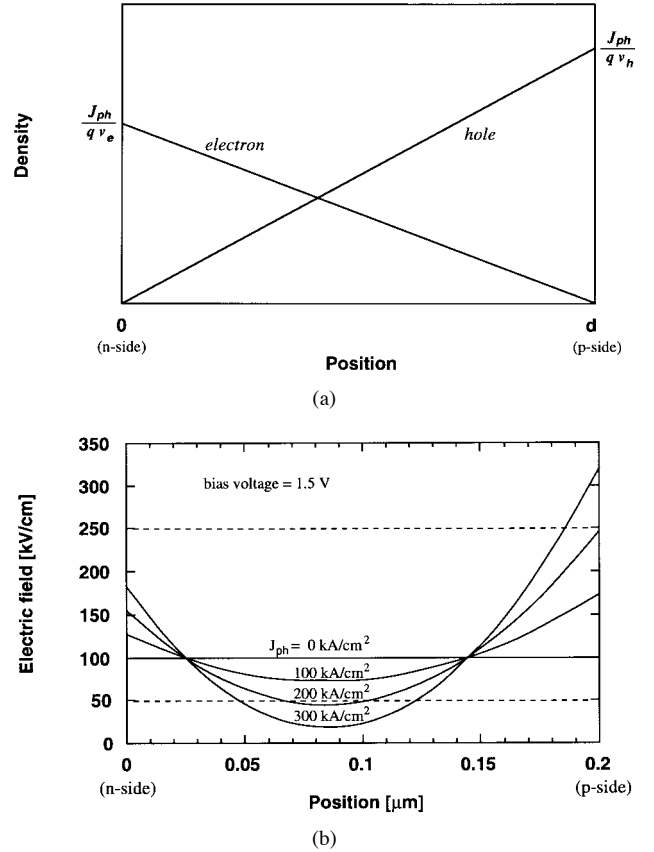


Fig. 8. (a) Carrier densities. (b) Electric fields at p-i-n PD.

carrier density becomes considerably high under high-power illumination. In other words, there is a tradeoff between the bandwidth and saturation current.

To obtain a general understanding of the space-charge effect, we first consider the maximum instantaneous carrier densities at an intrinsic InGaAs photoabsorption layer by assuming the carrier velocities are constant, as shown in Fig. 8(a), where J_{ph} is a maximum instantaneous density. (A rigid simulation would require a field-dependent carrier velocity, which was used in the previous works.) The electric fields E are then estimated by using Poisson's equation, as shown in Fig. 8(b), with J_{ph} as a parameter. Here, it is assumed that the light is illuminated uniformly over the whole volume, and the thickness d is 0.2 μm , bias voltage V_b is 1.5 V, the electron saturated velocity v_e is 6.5×10^6 cm/s [6], the hole saturated velocity v_h is 4.8×10^6 cm/s [6], and the background doping level is 1×10^{15} cm⁻³. One can see that each electric field has a minimum value at $x = dv_h/(v_e + v_h)$ due to the space-charge effect. Though the above estimation is based on a dc model, it can also provide a good approximation when the light is modulated at frequencies of much less than the carrier-transit-limiting bandwidth f_t . (In this case, since $f_t = 150$ GHz at $d = 0.2$ μm , the approximation could be adequate up to about 100 GHz.) For a modulated light, J_{ph} means the sum of the dc and the RF-peak current densities. If we assume that the critical electric field of the hole saturated velocity is 50 kV/cm [62], hole transit could not follow the modulation and nonlinearity will appear when J_{ph} is beyond 200 kA/cm², as shown in Fig. 8(b).

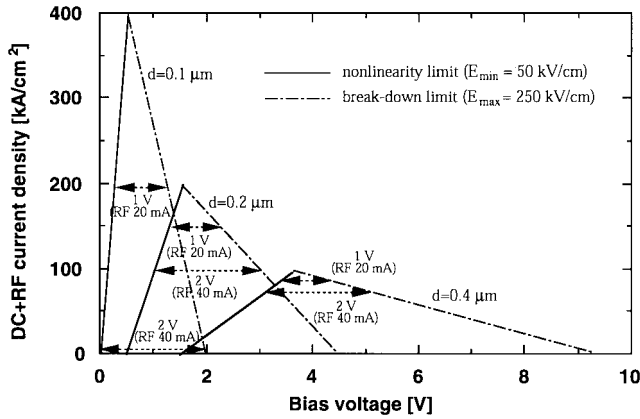


Fig. 9. Calculated saturation current at p-i-n PD.

It can be observed that the electric field has the maximum value at $x = d$ and this value increases as J_{ph} increases. Previous works found that breakdown occurs when the maximum field exceeds the critical value, which was determined to be 250 kV/cm [62], [63]. This is the second factor that limits the maximum available output current. It has also been found thermal destruction is a limiting factor [29], [52], [59], [62], [63]. The thermal effect is thought to be due to the consumed electrical power inside the PD [59]. (A general discussion here is difficult because the thermal diffusion constant strongly depends on the three-dimensional (3-D) structure. Hence, we will not discuss the thermal effect in this section. It will be estimated experimentally in Section IV.)

Based on the same analysis as that described in Fig. 8(b), we calculated the minimum and maximum electric fields (E_{min} and E_{max}) by using d and bias voltage V_b as parameters, and then ascertained the possible photocurrent density which satisfies $E_{min} > 50$ kV/cm and $E_{max} < 250$ kV/cm. The solid and broken lines in Fig. 9 show the critical current densities for $E_{min} = 50$ kV/cm and $E_{max} = 250$ kV/cm in 0.1-, 0.2-, and 0.4- μ m-thick photoabsorption layers. It is clear that, if we choose the optimized bias voltage, the maximum available current density increases when d decreases. However, in reality, the radio-frequency (RF) photocurrent induces a bias voltage drop due to the output 50- Ω impedance, as was found in [50], [52], and [63]. This voltage drop (1 V at a RF photocurrent I_{ph} of 20 mA and 2 V at 40 mA) is not negligible at a high photocurrent. Thus, for practical operation, the current density should be kept at a moderate level so that it does not jump over the limit even when the bias voltage drops. The lengths of the vertical arrows in Fig. 9 indicate the fluctuation of the bias voltage with RF photocurrents of 20 and 40 mA. (Precisely, the arrows would lie on the 50- Ω -load line when the modulation depth is 100%.) Thus, the vertical position of these arrows illustrates the possible current densities at RF photocurrents of 20 and 40 mA. One can see that the bias voltage drop is more dominant with a thinner photoabsorption layer. (The extreme case of $d = 0.1$ μ m and $I_{ph} = 40$ mA, J_{ph} would be allowed at only a few kA/cm².)

Thus, Fig. 9 can be used to design the PD dimensions for a current. As an example, the PD dimensions for a 40-mA current are designed as follows.

- 1) First, from the target RF current of 40 mA, a bias voltage drop of 2 V is estimated.
- 2) Then, $d = 0.2$ μ m is chosen because it provides a higher J_{ph} of 100 kA/cm² when a 2-V margin is considered.
- 3) Then, if the illumination is uniform, the possible area of (40 mA)/(100 kA/cm² = 40 μ m²) is deduced.
- 4) Finally, it is determined whether the CR time-limited bandwidth calculated with the above dimensions satisfies the desirable bandwidth. (If not, a distributed PD design would be required.)

In the case of uneven illumination, the saturation appears preferentially at the point where the current density is highest. For example, the J_{ph} near the input end of the WGPD is about three times as high as the average current, which results in reducing the maximum available current by a factor of three. Thus, uniform illumination is one way to improve the saturation current. It is also essential to decrease the average current density itself by enlarging the effective photoabsorption region through the use of the distributed device scheme. In the following discussions, several design challenges we face in improving the saturation current are discussed.

B. Structure Design Challenges

Although the general idea for improving the saturation current is to distribute the photoabsorption along a long waveguide, this degrades the bandwidth at the WGPD. Thus, there is a certain tradeoff between the saturation current and the bandwidth, as was predicted in [29]. The saturation current of the WGPD was first investigated in a 20-GHz device [55]. It was confirmed that there was no saturation with a dc current of up to about 4 mA. Numerical investigations on the WGPD were also reported [53], and they indicated that the saturation current is limited by the higher photocurrent near the input end due to exponential photoabsorption decay.

A tapered WGPD [distributed photoabsorption WGPD (DWGP)] was proposed [62] as one possible way to make the photoabsorption uniform along the WGPD. The DWGP has two main features: it has a very thin (0.06- μ m thick) photoabsorption layer embedded in laterally tapered transparent intrinsic layers and it has an underlying slab waveguide. In the DWGP, the optical confinement gradually increases along the waveguide by a factor of ten, which results in uniform photoabsorption. Experimental results showed that a 300- μ m-long p-i-n DWGP delivers a linear microwave photocurrent of 8 mA, as well as 20-GHz bandwidth at 1.53- μ m wavelength. (The dc current would be much greater than 8 mA.)

In the TWPD, there is the same feature of exponential decay of the photoabsorption as in the WGPD. Thus, in order to increase the saturation current, the photoabsorption should be distributed along the waveguide by decreasing $\Gamma\alpha$. However, as described in the previous section, the TWPD has a kind of lumped-element property due to the mismatching of electrical/optical waves. Thus, there is a tradeoff between saturation current and bandwidth. Since the TWPD without matched termination has a bandwidth similar to that of the WGPD with the same effective photoabsorption length as

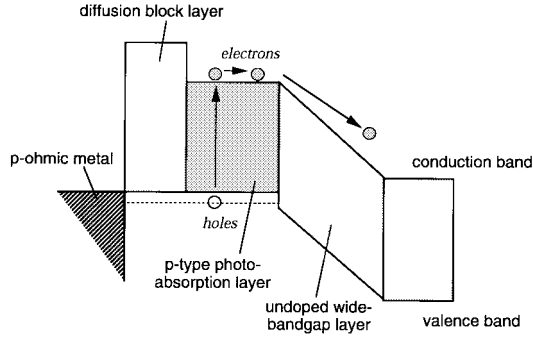


Fig. 10. Band diagram of UTC-PD.

described by (13), it also has a similar bandwidth-current limit. On the other hand, the TWPDP with matched termination has a bandwidth about 2–4 times as large as that of the unmatched TWPDP of WGPDP as described by (12). Thus, the TWPDP with matched termination can provide a saturation current 2–4 times as large as that of the WGPDP with the same bandwidth even though the efficiency is cut by half. Although an experimental estimation of the saturation current has not yet been reported, a trial experiment using a 1250- μm -long p-i-n TWPDP was conducted for a short wavelength [64].

The P-TWPDP should have a very high-saturation current if electrical/optical wave matching is performed. Simulated results showed saturation currents are about 50 and 20 mA in a P-TWPDP designed to have bandwidths of 50 and 100 GHz [29]. By measuring an impulse response at a short wavelength, it is found that when using the GaAs-MSM structure, the P-TWPDP achieved a peak saturation current of about 60 mA, as well as a bandwidth of 40 GHz [29]. Though the saturation current is overestimated if we use an impulse response because fewer carriers or fewer space charges are generated than when sinusoidally modulated light is used, the result indicates a considerable improvement of the saturation current compared to the impulse response of the WGPDP.

C. Carrier-Transport Design Challenges

As described above, the space-charge effect is caused by the low saturated velocity of carriers. If we could use electrons traveling at their overshoot speed, the saturation current would be significantly increased. The uni-traveling-carrier photodiode (UTC-PD) is based on this concept and was proposed in 1997 [65]. The UTC-PD is essentially based on a p-i-n structure having a p-type photoabsorption layer and a transparent wide-bandgap depletion layer, as shown in Fig. 10. The uni-traveling-carrier (UTC) mechanism is as follows. Holes generated in the photoabsorption layer are majority carriers, which respond very quickly with dielectric relaxation time, and thus do not contribute to the photocurrent. In contrast, electrons generated in the photoabsorption layer diffuse toward the depletion layer and drift across it, which causes them to contribute to the photocurrent. Thus, the space-charge effect is caused only by electrons traveling in the depletion layer. Furthermore, in a depletion layer thinner than 0.2 μm , electrons can drift at the overshoot velocity, which is five times higher than the saturation velocity. Thus, the carrier density

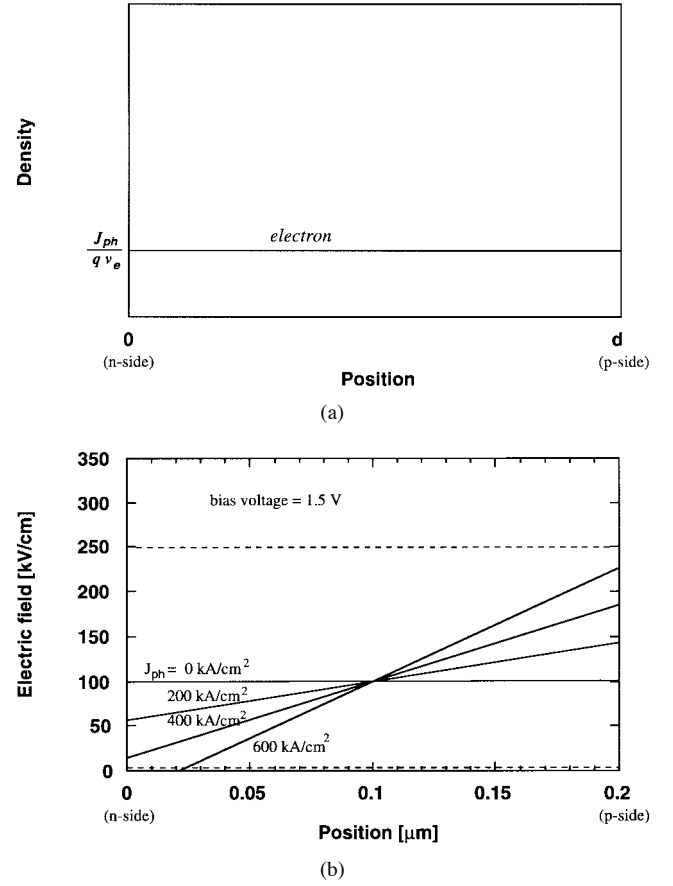


Fig. 11. (a) Carrier densities and (b) electric fields at UTC-PD.

in the depletion layer is one-fifth that with the conventional p-i-n structure.

As for the bandwidth, the electron diffusion time in the photoabsorption layer dominates the carrier-transit time. The diffusion time is proportional to the square of thickness d . (In contrast, the transit time is proportional to d in the conventional p-i-n structure.) Assuming that the depletion and photoabsorption layers have the same thickness d , the bandwidth of the UTC-PD is smaller than that of the conventional p-i-n PD when d is larger than 0.1 μm [65]. The effect of the quasi-electric-field caused by the conduction-band gradient is significant and can be used to improve the bandwidth. Only a 50-mV conduction-band gradient, which can be easily obtained by grading the material composition from that for a wider bandgap to that for narrower bandgap, can increase the bandwidth to that of the conventional structure [65].

To roughly estimate the space-charge effect at the UTC-PD, we first consider the electron density in the depletion layer, as shown in Fig. 11(a). Here, we assume that the overshoot velocity is constant at 4×10^7 cm/s while electrons are drifting inside a thin layer, which is estimated theoretically and testified experimentally at a 0.3- μm -thick InGaAs heterojunction bipolar transistors (HBT's) with low bias voltage [66]. (The value is somewhat higher than some reported "overshoot velocities" in thick layers.) We also assume that photogenerated electrons do not recombine and the light illumination is uniform. The uniform current flow shown here distinguishes the UTC-

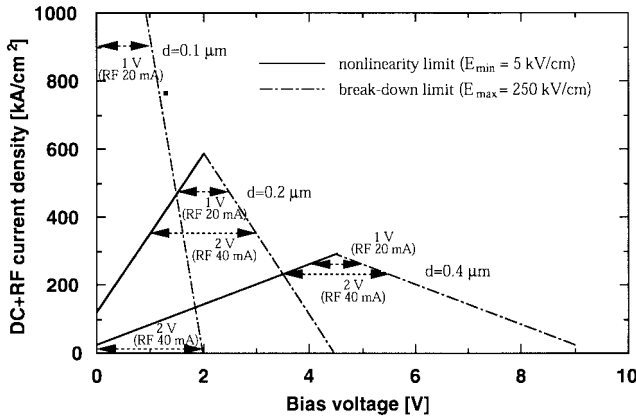


Fig. 12. Calculated saturation current at p-i-n PD.

PD. The electric fields E are then calculated as shown in Fig. 11(b), using the assumption that $d = 0.2 \mu\text{m}$, $V_b = 1.5 \text{ V}$, and background doping level is $1 \times 10^{15} \text{ cm}^{-3}$. (A more accurate profile should be obtained by using a field-dependent electron velocity and calculating the redistributed field and velocity self-consistently.) One can notice that E_{\min} appears at $x = 0$ (n-side edge). Since the electron velocity significantly decreases at the electric field of less than 5 kV/cm , the critical electric field for nonlinearity is assumed to be 5 kV/cm for the UTC-PD. The assumption that electrons drift at their overshoot velocity would be appropriate because of the low electric field around such a critical point. Next, we calculated E_{\min} and E_{\max} at the UTC-PD with d and V_b as parameters, and then ascertained the possible J_{ph} that satisfies $E_{\min} > 5 \text{ kV/cm}$ and $E_{\max} < 250 \text{ kV/cm}$. The solid and broken lines in Fig. 12 show the critical current densities for $E_{\min} = 5 \text{ kV/cm}$ and $E_{\max} = 250 \text{ kV/cm}$, at the 0.1-, 0.2-, and 0.4- μm -thick photoabsorption layers. One can see that J_{ph} looks similar to that of the conventional photodiode, but it actually has a value that is about three times larger. Furthermore, J_{ph} could be improved when we use a wider bandgap depletion layer (such as InP), which increases the E_{\max} . As for the thermal effect, the UTC-PD has a thermal-destruction limit that is similar to other lumped PD's. Thus, the saturation of the actual UTC-PD could be determined by this effect, as discussed in Section IV. Thus, our future work could focus on a distributed UTC-PD.

Recently, experimental results also have shown the excellent performance of UTC-PD's. A vertically illuminated UTC-PD with a 0.14- μm -thick graded-doping photoabsorption and 0.2- μm -thick depletion layers showed a pulse response with a peak photocurrent of 76 mA (1.9 V at 25- Ω load), a bandwidth of 114 GHz, and an efficiency of 13% [11]. Since a thin photoabsorption layer of less than 0.3 μm is essential for UTC operation [65], low efficiency is inevitable for the vertically illuminated UTC-PD. To improve the efficiency, a UTC structure was introduced into the WGPd [67]. When a double-core multimode waveguide and a mushroom-mesa structures were applied, the UTC-WGPd showed a pulse response with a peak photocurrent of 26 mA (1.3 V at 50- Ω load), a bandwidth of 55 GHz, and an efficiency of 32% [67].

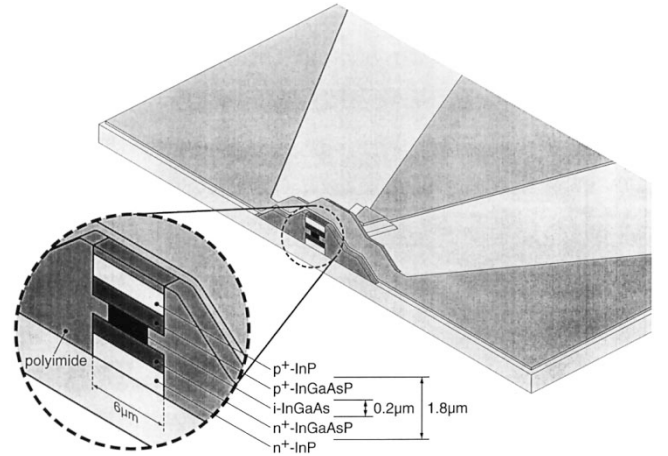


Fig. 13. Schematic view of fabricated WGPd.

IV. THE DEVELOPMENT OF PD'S

In this section, the key technologies for developing WGPd's and the performances of some recently developed WGPd's are summarized. The technologies focus not only on the processing of semiconductor layers, but also on module assembly because both are instrumental in obtaining high-quality PD's. In addition, we introduce recently developed monolithic receiver OEIC's and describe the state-of-the-art performance of a WGPd-based OEIC.

A. WGPd

As described in the previous section, theoretical results show an ultimate performance but, in reality, the experimentally observed performance is strictly limited by undesirable parasitic components such as series resistance, stray capacitance, and inductance. Especially serious is that when the photoabsorption-layer thickness is decreased in order to obtain more bandwidth, the capacitance increases and tradeoff becomes even more critical. Thus, in the fabrication of WGPd's, the focus has been mainly on eliminating these parasitic components by using selective mushroom-mesa etching for low resistance and burying the mesa with polyimide for low capacitance.

Fig. 13 shows the structure of long-wavelength WGPd's for 100-GHz bandwidth. The thickness of the InGaAs photoabsorption layers is designed to be 0.2 μm in order to achieve 100-GHz operation within a certain margin. The InGaAsP intermediate bandgap layers, which generate a multimode configuration, form a 1.8- μm -thick double core, so that the optical field distribution at a 1.8- μm -thick double core matches a lensed fiber. The 6- μm -wide waveguide mesa was formed by dry etching in BBr_3 followed by removal of 0.05- μm -thick damaged surface by isotropic chemical etching. Then, the photoabsorption layers were narrowed down to 0.8 or 1.5 μm by H_2SO_4 -based chemical etching. Experiments showed that the 6- μm -wide upper p-type and lower n-type layers provide series resistance of less than 10 Ω even with a 0.8- μm -wide mesa.

The p and n electrodes were formed on the upper and lower doped layers. In order to minimize the stray capacitance, the output lines connecting these electrodes were laid out on polyimide slopes adjacent to the mesa. The polyimide layer

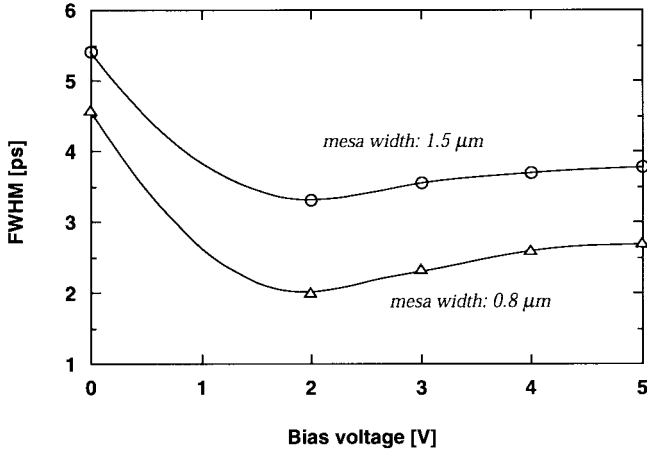


Fig. 14. Measured FWHM's of short pulse responses for WGPD.

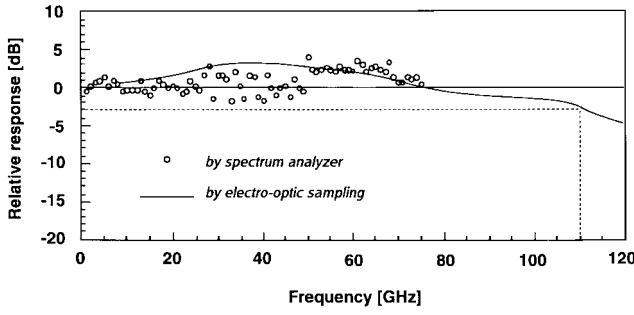


Fig. 15. Frequency responses of WGPD.

was spin-coated so that the thickness of the layer surrounding the mesa gradually decreases. The subsequent anisotropic etching of the polyimide layer results in moderate slopes around the mesa. Consequently, the device capacitances, including stray components, were 10 and 15 fF for the 0.8–1.5- μm -wide mesas. From these results, we estimated the bandwidths limited by the CR time constant to be 270 and 180 GHz, under a 50- Ω -load condition. Finally, the devices were cleaved to form 10- μm -long WGPD's, whose cleaved facets were coated with silicon nitride antireflection (AR) film.

The characterization of the WGPD chip was performed using an on-wafer probe head. The full width at half maximums (FWHM's) of a 1.55- μm -wavelength short-pulse response in both WGPD's are shown as a function of the bias voltage in Fig. 14. They were measured using electrooptic (EO) sampling [68]. The FWHM's had a bias dependence, and FWHM's of 2.0 ps for the 0.8- μm -wide mesa and 3.3 ps for the 1.5- μm -wide mesa were obtained at a reverse bias voltage of 2 V. The difference in the FWHM's indicates that the capacitance governs the bandwidth when the mesa is wider than 0.8 μm . The curve in Fig. 15 shows the Fourier transforms of the observed shortest pulse responses for the 1.5- μm -wide mesa and the dots are the frequency responses measured by a spectrum analyzer. The agreement between the results obtained by using different methods indicates the accuracy of the estimated 3-dB bandwidth of 110 GHz.

The measured efficiencies of the WGPD's were 20% for the 0.8- μm -wide mesa and 50% for the 1.5- μm -wide one when

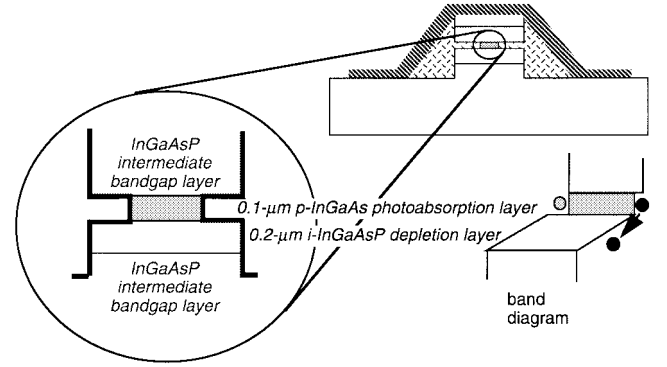


Fig. 16. Structure and band diagram of fabricated UTC-WGPD.

they were coupled to a hemispherically ended fiber. Thus, the bandwidth-efficiency product of the 1.5- μm -wide WGPD is 55 GHz. The difference from the calculated values is due to the coupling loss in the horizontal direction; the efficiency would reach about 80% if the input light had a smaller spot-size. A smaller spot-size can be obtained when we use a double-lens system inside a module, as described later in this section.

B. UTC-WGPD

We designed an UTC-WGPD structure aimed at a high-output current together with large bandwidth and high efficiency [67]. A UTC structure consisting of a 0.1- μm -thick p-type InGaAs photoabsorption layer and a 0.2- μm -thick undoped InGaAsP depletion layer was applied to a WGPD, as shown in Fig. 16. To form a double-core multimode waveguide, two 0.85- μm -thick intermediate bandgap layers were formed above and below the UTC structure. The upper intermediate bandgap layer also works as a diffusion block layer; it prevents the back diffusion of photogenerated electrons toward the p electrode.

Since the UTC structure was expected to provide a high-output current, the actual limiting factor might be the thermal effect rather than the space-charge effect. To clarify the limiting factor, we also fabricated a UTC-WGPD buried with a semiinsulating InP layer. A similar structure showed an enhanced thermal diffusion constant and then increased the maximum available optical input power of the electroabsorption modulator [69]. The fabrication process for the mushroom mesa UTC-WGPD is almost the same as that for the WGPD. To build the buried UTC-WGPD, first we formed a 1.5- μm -wide 10- μm -long mesa structure and then regrew a 3.5- μm -thick Fe-doped InP layer around the mesa [70]. The input facet was formed by cleaving the InP burying layer so that the light was illuminated through it into the WGPD layer.

Due to the inadequate doping of the lower intermediate bandgap layer, the parasitic resistance at the n side of the fabricated mesa-type and buried-type UTC-WGPD's is about 80 Ω . Furthermore, the buried UTC-WGPD has an additional parasitic resistance of 70 Ω at the p side because it does not employ a mushroom structure. Consequently, the total parasitic resistances is 80 Ω for the mushroom structure and 150 Ω for the buried one.

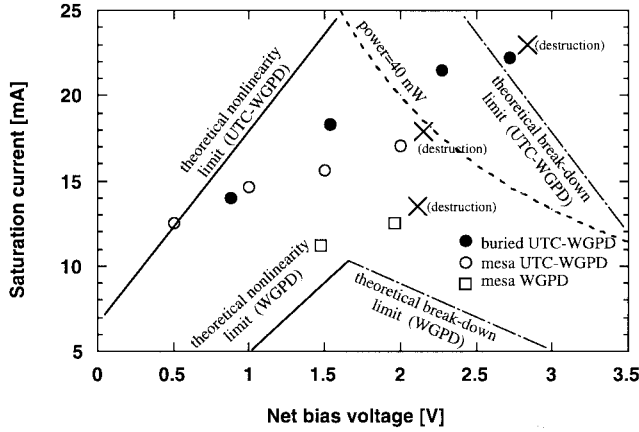


Fig. 17. Measured and calculated saturation currents of WGPD, UTC-WGPD, and buried UTC-WGPD.

First, we investigated the saturation and destruction currents when we input a continuous wave (CW) light power and detected the dc photocurrent. Fig. 17 shows the measured saturation currents of the mushroom-mesa UTC-WGPD (open circles) [67], the buried UTC-WGPD (closed circles) [70], and the mushroom-mesa WGPD (squares, as a reference) as functions of the net bias voltage that results from the subtraction of the voltage drop due to series resistance. These three devices have the same junction area of $1.5 \times 10 \mu\text{m}^2$ and photoabsorption thickness of $0.2 \mu\text{m}$. For both the mesa and buried UTC-WGPD, the measured saturation currents are in a similar position and they are 1.5 times as large as that for the WGPD under the same bias condition. The upper solid line shows the nonlinearity limit for the UTC-WGPD, which was deduced from the result in Fig. 12, assuming that J_{ph} near the input end is three times as large as that in the case of uniform absorption. Though the mechanism of dc compression is not the same as that of RF [71], both should be triggered by the carrier-velocity lowering under the same critical condition. This is why the measured dc saturation current has the trend similar to the theoretical line for RF. The crosses in the figure show the point where each device was destroyed. Since the mesa-type UTC-WGPD should have the same breakdown limit as that of the buried-type (because they have the same UTC structure), the destruction of the mesa-type is thought to be due to the thermal effect. Thus, the thermal destruction limit for our mushroom-mesa device corresponds to a current-voltage product of around 40 mW and that for the buried device has a higher limit. The buried UTC-WGPD reaches a saturation current of around 22 mA and breaks down near the theoretical breakdown limit (upper broken line). Thus, using the buried structure, we can make full use of the UTC performance.

As for the conventional WGPD, the device breaks down before reaching the 40-mW curve (dot curve). This means that the saturation of the conventional WGPD is dominated by the breakdown limit and the limit is much lower than that for the UTC-WGPD. This feature is consistent with the discussion in Section III, although the theoretical limit deduced from the results in Fig. 12 (solid and broken lines) is lower than the experimental limit.

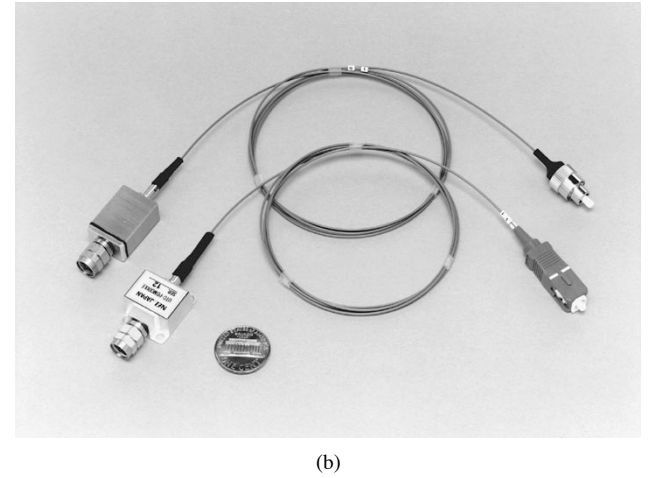
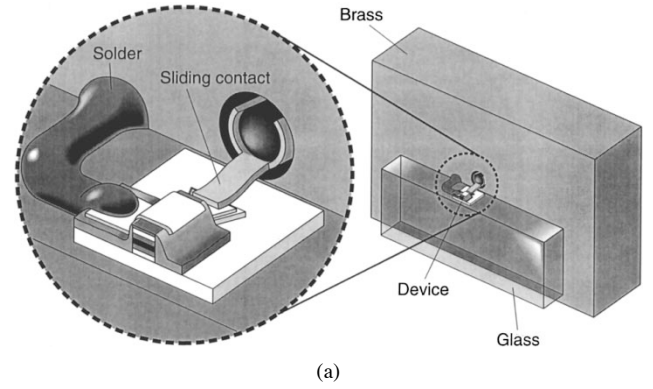


Fig. 18. 60-GHz-package configuration: (a) inside and (b) outside (WGPD and UTC-WGPD).

Next, we measured the $1.55\text{-}\mu\text{m}$ -wavelength response pulse of the mushroom-mesa multimode UTC-WGPD using an on-wafer probe-head. The 3-dB bandwidth was estimated to be 55 GHz from the Fourier transform of the measured response pulse [67]. The main bandwidth limiting factor was the CR time constant because of the high parasitic resistance of 80Ω . Appropriate doping of the lower intermediate bandgap layer would fully exploit the UTC-WGPD and push the bandwidth up into the 100-GHz region. When the UTC-WGPD was coupled to a hemispherically ended fiber, the measured efficiency was 50% [67], which is almost the same as that of the conventional WGPD.

C. Ultrawide-Bandwidth Packaging

Here, we describe a mounting technology based on the 60-GHz Wiltron V connector. For 60-GHz operation in a $50\text{-}\Omega$ system, the device capacitance, including stray capacitance, must be less than 50 fF in terms of the CR time constant, which is much larger than the photodiode capacitance of 15 fF. Thus, we use the lumped-designed bonding pad, whose capacitance is 20 fF, instead of a coplanar line. Consequently, the total capacitance was about 35 fF, which is low enough for 60-GHz operation. The main concern then became how to reduce additional parasitic components originating from packaging. For this purpose, we developed the package configuration shown in Fig. 18(a). This configuration features direct bonding to the

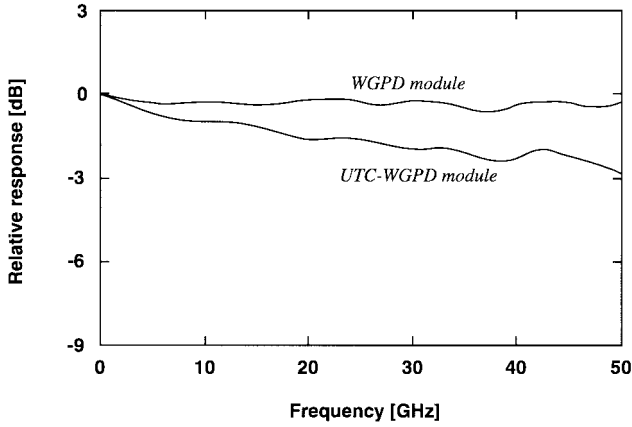


Fig. 19. Frequency responses of WGPD and UTC-WGPD.

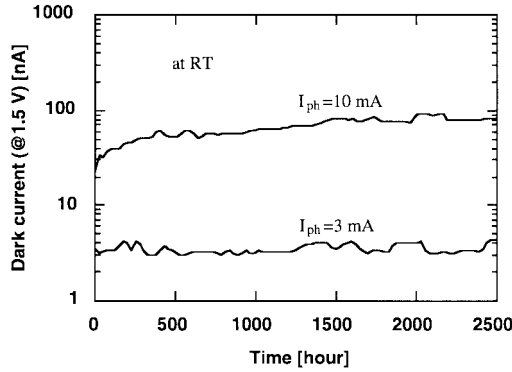


Fig. 20. Life test of packaged WGPD and UTC-WGPD at room temperature. Small variations are due to variation of the room temperature.

center conductor using a commercial Wiltron sliding contact and mounting on a glass substrate, both of which minimize the additional capacitance and inductance resulting from the packaging. The optical interface to a single-mode fiber consists of a collimating and focusing lens. These lenses were fixed to the metal main package using a yttrium–aluminum–garnet (YAG) laser welder. The spot size of the focused light was about $1\ \mu\text{m}$. Finally, the package was encapsulated with a metal cover, as shown in Fig. 18(b).

The frequency response at -1.5-V bias of a typical WGPD module has a bandwidth of more than 50 GHz, while that of the UTC-WGPD has a bandwidth of around 50 GHz, as shown in Fig. 19. The smaller bandwidth of the UTC-WGPD is due to the higher parasitic resistance, as described earlier. The efficiencies were typically 64% (0.8 A/W) and a maximum of 80% (1 A/W) for both the WGPD and UTC-WGPD. As for the reliability, we tested the packaged device by continuously feeding optical power for 2500 h at room temperature. In this test, the optical powers were controlled so as to generate 3-mA dc photocurrent at the WGPD and 10 mA at the UTC-WGPD. Neither the WGPD nor the UTC-WGPD exhibited any degradation of efficiency. This confirmed the high reliability of the optical coupling. Dark currents did not increase in the WGPD, while they gradually increased in the UTC-WGPD, as shown in Fig. 20. The degradation of the UTC-WGPD is thought to be due not to breakdown, but to the thermal effect because the limiting factor for the mesa-type UTC-WGPD is

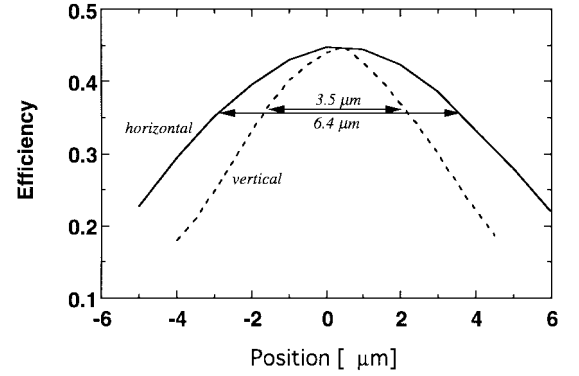


Fig. 21. Measured efficiencies of 20-GHz WGPD as functions of misalignment distance.

the thermal destruction, as described above. This means that the buried-type UTC-WGPD would be more stable in the same reliability test.

The coupling technology described here has also been applied to a 40-Gb/s hybrid WGPD-AMP [72] and a 72-GHz WGPD-based stimulus probe head [73]. These devices also demonstrated good efficiency, which indicates that this coupling technology is well-suited to WGPD's.

D. Large-Core WGPD and Its PLC-Hybrid Integration

For the integration of a PD with other optical functions, platform technology based on the planar lightwave circuit (PLC) is a powerful candidate. It reduces the number of assembled components of the module [74] and, since the WGPD has an edge-coupling scheme that is compatible with the PLC, it dramatically reduces module cost. Here, we present the fabrication and performance of a 20-GHz WGPD designed for a PLC-hybrid differential receiver.

The basic structure is almost the same as that of the 100-GHz WGPD, but each layer is optimized to obtain a high efficiency with a PLC. The InGaAs photoabsorption layer was $1.1\text{-}\mu\text{m}$ thick and the InGaAsP intermediate bandgap layers form a $3.1\text{-}\mu\text{m}$ -thick double core that generates a multimode configuration and matches the optical field distributions at a PLC.

Fig. 21 shows the measured efficiencies as functions of misalignment distance when the WGPD is coupled to a cleaved dispersion shifted fiber whose optical field is similar to that of the PLC. The peak responsivity is as high as 45% and there are large 1-dB-down misalignment tolerances of 3.5 and $6.4\ \mu\text{m}$ in the vertical and horizontal directions. Two WGPD's were serially jointed to form a dual WGPD and were mounted on the PLC platform using solder bumps, as shown in Fig. 22. In this PLC, the incoming light is divided into two guided lights, one of which is delayed by a half bit inside the longer waveguide. Each light is then injected into each WGPD, which then generates the differential signal. The dual-WGPD mounted on the PLC had a bandwidth of 22 GHz and could detect a 12-Gb/s differential Manchester-coded signal with a high efficiency of 40%. From these results, and owing to the simplicity of coupling to a PLC without any additional components such as lenses or mirrors, one can expect that

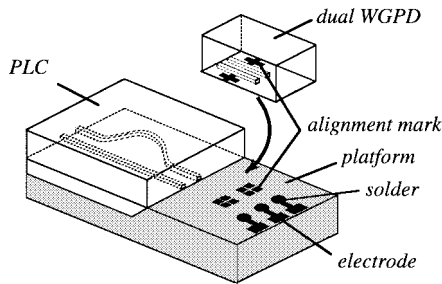


Fig. 22. Schematics of PLC-integration of dual 20-GHz WGP.

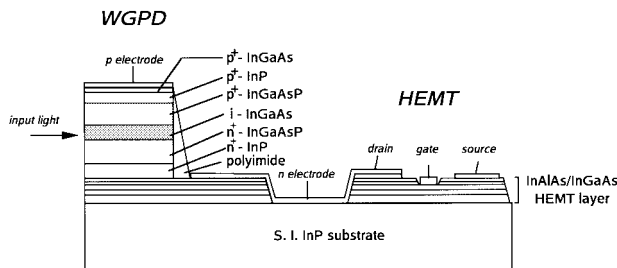


Fig. 23. Cross-sectional structure of WGP-HEMT receiver OEIC.

the WGP is also suitable for PLC-hybrid integration with a speed of up to 20 GHz.

E. Receiver OEIC

The complexity of the assembly mainly determines the cost of high-speed components. Monolithic OEIC's have been intensively investigated as way to construct low-cost receivers. An OEIC aiming at a larger bandwidth first reached the 20-Gb/s region with InP/InGaAs HBT's and a p-i-n VPD in 1994 [75]. Since then, several OEIC's, such as the p-i-n VPD/HBT [76], [77], p-i-n VPD/high electron-mobility transistor (VPD/HEMT) [78], and MSM VPD/HEMT [79], have been developed. These OEIC's consist of VPD's and lumped-designed circuits, such as trans-impedance or high-impedance amplifiers, which provide good performance as 20-Gb/s receivers.

For more bandwidth, both the PD and electric circuit should have configurations that allow them to operate at a desired bandwidth. Like the wide-band PD, the distributed amplifier (which itself had been reported to operate at 90 GHz [80]), was the key to enlarging the bandwidth. The 40-Gb/s OEIC was first demonstrated by using a WG-fed-PD and the HEMT-based distributed amplifier in 1996 [81] and then by using a WGP and the HEMT-based distributed amplifier in 1997 [82]. These new technologies have continued to increase the bandwidth and, very recently, 50-Gb/s operation has been observed [83], [84].

We present here the performance of a receiver OEIC consisting of a WGP and an InAlAs/InGaAs-HEMT-based distributed preamplifier. The WGP structure and the HEMT layers were designed individually and grown in piles, as shown in Fig. 23, so that each device would perform optimally even after integration. The WGP consists of a 2.15- μm -thick double-core multimode structure with a 0.35- μm -thick

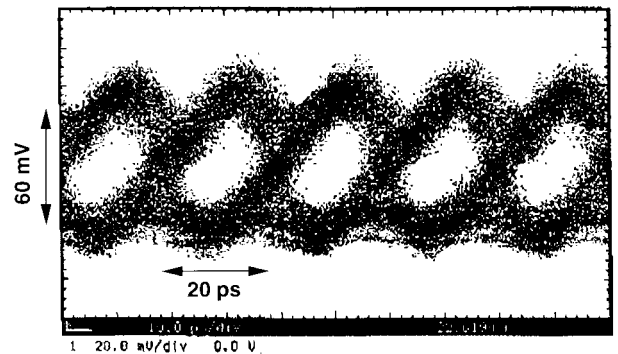


Fig. 24. Eye diagram observed from receiver OEIC for 50-Gb/s.

photoabsorption layer to provide a bandwidth of over 50 GHz, as well as high efficiency. The carrier-supplying InAlAs layer of the HEMT is Si planar doped to achieve high transconductance and excellent threshold-voltage uniformity. The HEMT has 0.5- μm -long gates composing an eight-section distributed amplifier [84].

The receiver OEIC without an AR coat has a bandwidth of 46.5 GHz and an efficiency of 40% at 1.55- μm wavelength and a transimpedance of 39-dB $\cdot\Omega$ [84]. The OEIC module was packaged using coupling technology similar to that used for the package for the 50-GHz WGP. For a 50-Gb/s-RZ signal, a clear eye opening was observed, as shown in Fig. 24.

These results show how each device can retain its individual performance even after monolithic integration. Since this OEIC included 16 HEMT's, a variety of microwave and millimeter-wave circuits on a similar scale could probably be integrated with a WGP by using this technology.

V. CONCLUSION

For PD's, the two main challenges are increasing the bandwidth-efficiency product and obtaining a high saturation current. The estimated bandwidth-efficiency products are similar for the WGP, TWP, and P-TWP. Experimentally, the highest bandwidth-efficiency products have been obtained with the WGP and TWP (for bandwidths of 50–200 GHz), the RFPD (for around 40 GHz), the APD (for around 20 GHz) and the RCE-PD, which has shown good potential over the whole range. For high saturation current, the space-charge effect must be reduced, and there are two approaches for doing this. One involves distributing the photocarriers along the light propagation direction in the WGP or TWP (which means we have to make a tradeoff between the saturation current and bandwidth) and in the P-TWP (which has an inherently high saturation current). The other approach is to increase the carrier velocity using the UTC structure, which would improve the saturation current by a factor of three. Experimentally, both P-TWP and UTC-PD showed the possibility of achieving a higher saturation current (60 mA and more) than conventional structures.

WGP-based fabrication technologies are applicable for a wide range—from a 20-GHz large-core WGP to a 100-GHz WGP and UTC-WGP. A 60-GHz packaging technol-

ogy for the edge-coupling photodiodes has been established, which enabled the development of reliable WGPd and UTC-WGPd modules. These technologies were also applied to the WGPd-based receiver OEIC. Integrated with a distributed amplifier, the WGPd made it possible to push OEIC operation to the 50-Gb/s region.

ACKNOWLEDGMENT

The author thanks Y. Muramoto, K. Takahata, M. Yuda, S. Hata, and H. Fukano for discussions, device design, fabrication, and measurement, N. Shimizu, and T. Ishibashi for the UTC design, M. Yaita and T. Nagatsuma for the EO sampling, A. Kozen, M. Mitsuhashi, R. Iga, and H. Sugiura for the epitaxial growth, Y. Ohkubo for proofreading of the manuscript, and O. Nakajima, Y. Matsuoka, M. Naganuma, and J. Yoshida for their continuous encouragement.

REFERENCES

- [1] M. Yaita, T. Nagatsuma, K. Kato, K. Noguchi, H. Miyazawa, and T. Otsuji, "Ultrafast optical signal measurement using optoelectronic techniques," *Opt. Quantum Electron.*, vol. 30, pp. 1119–1133, 1998.
- [2] H. Ogawa and D. Polifko, "Fiber optic millimeter-wave subcarrier transmission links for personal radio communication systems," in *IEEE MTT-S Symp. Dig.*, 1992, pp. 555–558.
- [3] H. Schmuck, R. Hofstetter, and R. Heidemann, "Advanced fiber-optic distribution of 140 Mbit/s mm-wave signals at 36 GHz," in *ECOC'94*, 1994, pp. 41–44.
- [4] K. Hagimoto, Y. Miyamoto, T. Kataoka, H. Ichino, and O. Nakajima, "20-Gbit/s signal transmission using a simple high-sensitivity optical receiver," in *OFC'92*, 1992.
- [5] K. Kato, K. Kawano, and A. Kozen, "Design of ultrawide-band, high-sensitivity p-i-n photodetectors," *IEICE Trans. Electron.*, vol. E76-C, pp. 214–221, 1993.
- [6] J. Bowers and C. Burrus, "Ultrawide-band long-wavelength p-i-n photodetectors," *J. Lightwave Technol.*, vol. LT-5, pp. 1339–1350, Oct. 1987.
- [7] K. Kishino, M. Ünlü, J. Chyi, J. Reed, L. Arsenault, and H. Morkoç, "Resonant cavity-enhanced (RCE) photodetectors," *IEEE J. Quantum Electron.*, vol. 27, pp. 2025–2034, Aug. 1991.
- [8] R. S. Tucker, A. J. Taylor, C. A. Burrus, G. Eisenstein, and J. M. Wisenfeld, "Coaxially mounted 67 GHz bandwidth InGaAs pin photodiode," *Electron. Lett.*, vol. 22, pp. 917–918, 1986.
- [9] Y. Wey, K. Giboney, J. Bowers, M. Rodwell, P. Silvestre, P. Thiagarajan, and G. Robinson, "108-GHz GaInAs/InP p-i-n photodiodes with integrated bias tees and matched resistors," *IEEE Photon. Technol. Lett.*, vol. 5, pp. 1310–1312, Nov. 1993.
- [10] I. Tan, C. Sun, K. S. Giboney, J. E. Bowers, E. L. Hu, B. I. Miller, and R. J. Capik, "120-GHz long-wavelength low-capacitance photodetector with an air-bridged coplanar metal waveguide," *IEEE Photon. Technol. Lett.*, vol. 7, pp. 1477–1479, Dec. 1995.
- [11] N. Shimizu, N. Watanabe, T. Furuta, and T. Ishibashi, "High-speed InP/InGaAs uni-traveling-carrier photodiodes with 3-dB bandwidth over 150 GHz," in *Device Res. Conf.'97*, 1997, Fort Collins, CO.
- [12] J. E. Bowers, and C. A. Burrus, "High-speed zero-bias waveguide photodetectors," *Electron. Lett.*, vol. 22, pp. 905–906, 1986.
- [13] K. Kato, S. Hata, A. Kozen, and J. Yoshida, "High-efficiency waveguide InGaAs p-i-n photodiode with bandwidth of greater than 40 GHz," in *OFC'91*, 1991.
- [14] D. Wake, T. P. Spooner, S. D. Perrin, and I. D. Henning, "50 GHz InGaAs edge-coupled pin photodetector," *Electron. Lett.*, vol. 27, pp. 1073–1075, 1991.
- [15] K. Kato, S. Hata, A. Kozen, J. Yoshida, and K. Kawano, "Highly efficient 40 GHz waveguide InGaAs p-i-n photodiode employing multimode waveguide structure," *IEEE Photon. Technol. Lett.*, vol. 3, pp. 820–822, Sept. 1991.
- [16] G. Hasnain, C. Madden, V. Robbins, and C. Su, "Fast, efficient and highly linear InGaAlAs waveguide pin photodetectors," in *InP and Related Materials'94*, 1994.
- [17] K. Kato, S. Hata, K. Kawano, J. Yoshida, and A. Kozen, "A high-efficiency 50 GHz InGaAs multimode waveguide photodetector," *IEEE J. Quantum Electron.*, vol. 28, pp. 2728–2735, Dec. 1992.
- [18] G. Wanlin, L. Giraudet, J. P. Praseuth, A. Miras, and E. Legros, "High responsivity side illuminated AlGaInAs pin photodiode for 40 Gbit/s-40 GHz applications," in *ECOC'97*, vol. 2, 1997, pp. 37–40.
- [19] K. Kato and J. Yoshida, "Ultrawide-bandwidth 1.55- μ m waveguide p-i-n photodiode," *Proc. SPIE-Int. Soc. Opt. Eng.*, vol. 2149, pp. 312–319, 1994.
- [20] K. Kato, A. Kozen, Y. Muramoto, Y. Itaya, T. Nagatsuma, and M. Yaita, "110-GHz, 50% efficiency mushroom-mesa waveguide p-i-n photodiode for a 1.55-mm wavelength," *IEEE Photon. Technol. Lett.*, vol. 6, pp. 719–721, June 1994.
- [21] J. G. Bauer, M. Schier, G. Ebbinghaus, and N. Emeis, "High responsivity integrated tapered waveguide pin photodiode," in *ECOC'93*, 1993.
- [22] K. Kato, S. Hata, J. Yoshida, and A. Kozen, "Design of a high-speed and high-sensitivity photodiode with an input optical waveguide on semi-insulating InP substrate," in *Int. Conf. Indium Phosphide Related Materials*, 1992.
- [23] S. Chandrasekhar, J. C. Campbell, F. G. Storz, A. G. Dentai, C. H. Joyner, and G. J. Qua, "Integrated balanced mixer circuit for coherent lightwave receivers," in *IGWO'89*, 1989.
- [24] K. Kato, S. Hata, A. Kozen, S. Oku, S. Matsumoto, and J. Yoshida, "22 GHz photodiode monolithically integrated with optical waveguide on semi-insulation InP using novel butt-joint structure," *Electron. Lett.*, vol. 28, pp. 1140–1141, 1992.
- [25] G. Unterbörnsch, A. Umbach, D. Trommer, and G. G. Mekonnen, "70 GHz long wavelength photodetector," in *ECOC'97*, vol. 2, 1997, pp. 25–28.
- [26] H. F. Taylor, O. Eknayan, C. S. Park, K. N. Choi, and K. Chang, "Traveling wave photodetectors," *Optoelectron. Signal Processing Phased-Array Antennas II*, pp. 59–63, 1990.
- [27] C. L. Goldsmith, G. A. Magel, B. M. Kanack, and R. J. Baca, "Coherent combining of RF signals in a traveling-wave photodetector array," *IEEE Photon. Technol. Lett.*, vol. 9, pp. 988–990, July 1997.
- [28] K. Giboney, M. Rodwell, and J. Bowers, "Traveling-wave photodetectors," *IEEE Photon. Technol. Lett.*, vol. 4, pp. 1363–1365, Dec. 1992.
- [29] L. Y. Lin, M. C. Wu, T. Itoh, T. A. Vang, R. E. Muller, D. L. Sivco, and A. Y. Cho, "High-power high-speed photodetectors design, analysis, and experimental demonstration," *IEEE Trans. Microwave Theory Tech.*, vol. 45, pp. 1320–1331, Aug. 1997.
- [30] K. S. Giboney, M. J. W. Rodwell, and J. E. Bowers, "Traveling-wave photodetector theory," *IEEE Trans. Microwave Theory Tech.*, vol. 45, pp. 1310–1319, Aug. 1997.
- [31] K. Giboney, R. Nagarajan, T. Reynolds, S. Allen, R. Mirin, M. Rodwell, and J. Bowers, "Traveling-wave photodetectors with 172-GHz and 76-GHz bandwidth-efficiency product," *IEEE Photon. Technol. Lett.*, vol. 7, pp. 412–414, Apr. 1995.
- [32] M. Alles, T. Braasch, and D. Jäger, "Traveling wave photodetector for optical generation of microwave signals," in *Int. Conf. Indium Phosphide Related Materials*, 1996.
- [33] M. Wu and T. Itoh, "Ultrafast photonic-to-microwave transformer (PMT)," in *IEEE LEOS Summer Topical Meeting Dig. Optical Microwave Interactions*, 1993.
- [34] E. Dröge, E. H. Böttcher, S. Kollakowski, A. Strittmatter, O. Reimann, R. Steingrüber, A. Umbach, and D. Bimberg, "Distribute MSM photodetectors for the long-wavelength range," in *ECOC'98*, vol. 1, 1998, pp. 20–24.
- [35] A. Chin and T. Y. Chang, "Multilayer reflectors by molecular-beam epitaxy for resonance enhanced absorption in thin high-speed detectors," *J. Vac. Sci. Technol.*, vol. 8, pp. 339–342, 1990.
- [36] M. S. Ünlü, K. Kishino, J. I. Chyi, L. Arsenault, J. Reed, S. N. Mohammad, and H. Morkoç, "Resonant cavity enhanced AlGaAs/GaAs heterojunction phototransistors with an intermediate InGaAs layer in the collector," *Appl. Phys. Lett.*, vol. 57, pp. 750–752, 1990.
- [37] J. C. Campbell, "Resonant-cavity photodetectors," in *Int. Electron Devices Meeting*, 1995.
- [38] C. C. Barron, C. J. Mahon, B. J. Thibault, G. Wang, W. Jiang, L. A. Coldren, and J. E. Bowers, "Resonant-cavity-enhanced pin photodetector with 17 GHz bandwidth-efficiency product," *Electron. Lett.*, vol. 30, pp. 1796–1797, 1994.
- [39] B. M. Onat, M. Gökkavas, E. Özbay, E. P. Ata, E. Towe, and M. S. Ünlü, "100-GHz resonant cavity enhanced Schottky photodiodes," *IEEE Photon. Technol. Lett.*, vol. 10, pp. 707–709, May 1998.
- [40] I. Tan, J. Dudley, D. Babic, D. Cohen, B. Young, E. Hu, J. Bowers, B. Miller, U. Koren, and M. Young, "High quantum efficiency and narrow absorption bandwidth of the wafer-fused resonant In_{0.53}Ga_{0.47}As photodetectors," *IEEE Photon. Technol. Lett.*, vol. 6, pp. 811–813, July 1994.
- [41] H. Fukano, A. Kozen, K. Kato, and O. Nakajima, "Edge-illuminated

- refracting-facet photodiode with high responsivity and low-operation voltage," *Electron. Lett.*, vol. 32, pp. 2346–2347, 1996.
- [42] H. Fukano, K. Kato, O. Nakajima, and Y. Matsuoka, "Low-cost, high-speed and high-responsivity edge-illuminated refracting-facet photodiode module," in *OECC'98*, 1998.
 - [43] J. C. Campbell, B. C. Johnson, G. I. Qua, and W. T. Tsang, "Frequency response of InP/InGaAsP/InGaAs avalanche photodiodes," *J. Lightwave Technol.*, vol. 7, pp. 778–784, May 1989.
 - [44] T. Kagawa, Y. Kawamura, and H. Iwamura, "InGaAsP-InAlAs superlattice avalanche photodiode," *IEEE J. Quantum Electron.*, vol. 28, pp. 1419–1423, June 1992.
 - [45] ———, "A wide-bandwidth low-noise InGaAsP-InAlAs superlattice avalanche photodiode with a flip-chip structure for wavelengths of 1.3 and 1.55 μm ," *IEEE J. Quantum Electron.*, vol. 29, pp. 1387–1392, May 1993.
 - [46] M. Shishikura, H. Nakamura, S. Hanatani, S. Tanaka, T. Miyazaki, and S. Tsuji, "An InAlAs/InGaAs superlattice avalanche photodiode with a waveguide structure," in *OECC'94*, 1994.
 - [47] C. Cohen-Jonathan, L. Giraudet, A. Bonzo, and J. P. Praseuth, "Waveguide AllnAs avalanche photodiode with a gain-bandwidth product over 160 GHz," *Electron. Lett.*, vol. 33, pp. 1492–1493, 1997.
 - [48] R. Kuchibhotla, A. Srinivasan, J. C. Campbell, C. Lei, D. G. Deppe, Y. S. He, and B. G. Streetman, "Low-voltage high-gain resonant-cavity avalanche photodiode," *IEEE Photon. Technol. Lett.*, vol. 3, pp. 354–356, Apr. 1991.
 - [49] H. Nie, K. A. Anselm, C. Hu, S. S. Murtaza, B. G. Streetman, and J. C. Campbell, "High-speed resonant-cavity separate absorption and multiplication avalanche photodiodes with 130 GHz gain-bandwidth product," *Appl. Phys. Lett.*, vol. 70, pp. 161–163, 1997.
 - [50] M. Dentan and B. D. Cremoux, "Numerical simulation of the nonlinear response of a p-i-n photodiode under high illumination," *J. Lightwave Technol.*, vol. 8, pp. 1137–1144, Aug. 1990.
 - [51] E. H. Böttcher, E. Dröge, D. Bimberg, A. Umbach, and H. Engel, "Ultra-wide-band (>40 GHz) submicron InGaAs metal-semiconductor-metal photodetectors," *IEEE Photon. Technol. Lett.*, vol. 8, pp. 1226–1228, Sept. 1996.
 - [52] K. J. Williams, R. D. Esman, and M. Dagenais, "Nonlinearities in p-i-n microwave photodetectors," *J. Lightwave Technol.*, vol. 14, pp. 84–96, Jan. 1996.
 - [53] J. Harari, F. Journet, O. Rabii, G. Jin, J. P. Vilcot, and D. Decoster, "Modeling of waveguide PIN photodetectors under very high optical power," *IEEE Trans. Microwave Theory Tech.*, vol. 43, pp. 2304–2310, Sept. 1995.
 - [54] J. Harari, G. H. Jin, F. Journet, J. Vandecasteele, J. P. Vilcot, C. Dalle, M. R. Friscourt, and D. Decoster, "Modeling of microwave top illuminated PIN photodetector under very high optical power," *IEEE Trans. Microwave Theory Tech.*, vol. 44, pp. 1484–1487, Aug. 1996.
 - [55] A. R. Williams, A. L. Kellner, X. S. Jiang, and P. K. L. Yu, "InGaAs/InP waveguide photodetector with high saturation intensity," *Electron. Lett.*, vol. 28, pp. 2258–2259, 1992.
 - [56] A. R. Williams, A. L. Kellner, and P. K. L. Yu, "High frequency saturation measurements of an InGaAs/InP waveguide photodetector," *Electron. Lett.*, vol. 29, pp. 1298–1299, 1993.
 - [57] D. Kuhl, F. Hieronymi, E. H. Böttcher, T. Wolf, D. Bimberg, J. Kuhl, and M. Klingenstein, "Influence of space charges on the impulse response of InGaAs metal-semiconductor-metal photodetectors," *J. Lightwave Technol.*, vol. 10, pp. 753–759, 1992.
 - [58] R. R. Hayes, and D. L. Persechini, "Nonlinearity of p-i-n photodetectors," *IEEE Photon. Technol. Lett.*, vol. 5, pp. 70–72, Jan. 1993.
 - [59] J. S. Paskalski, P. C. Chen, J. S. Chen, C. M. Gee, and N. Bar-Chaim, "High-power microwave photodiode for improving performance of RF fiber optic links," *Proc. SPIE*, vol. 2844, pp. 110–119, 1996.
 - [60] R. B. Welstand, H. Jiang, J. T. Zhu, Y. Z. Liu, S. A. Pappert, and P. K. L. Yu, "High-speed and high-saturation power semiconductor waveguide photodetector structures," in *OFC'97*, 1997.
 - [61] K. J. Williams, R. D. Esman, R. B. Wilson, and J. D. Kulick, "Differences in p-side and n-side illuminated p-i-n photodiode nonlinearities," *IEEE Photon. Technol. Lett.*, vol. 10, pp. 132–134, Jan. 1998.
 - [62] S. Jasmin, N. Vodjdani, J. Renaud, and A. Enard, "Diluted and distributed-absorption microwave waveguide photodiodes for high efficiency and high power," *IEEE Trans. Microwave Theory Tech.*, vol. 45, pp. 1337–1341, Aug. 1997.
 - [63] J. Harari, G. Jin, J. P. Vilcot, and D. Decoster, "Theoretical study of p-i-n photodetectors' power limitations from 2.5 to 60 GHz," *IEEE Trans. Microwave Theory Tech.*, vol. 45, pp. 1332–1336, Aug. 1997.
 - [64] V. M. Hietala, G. A. Vawter, T. M. Brennan, and B. E. Hammons, "Traveling-wave photodetectors for high-power, large bandwidth applications," *IEEE Trans. Microwave Theory Tech.*, vol. 43, pp. 2291–2297, Sept. 1995.
 - [65] T. Ishibashi, N. Shimizu, S. Kodama, H. Ito, T. Nagatsuma, and T. Furuta, "Uni-traveling-carrier photodiodes," *Ultrafast Electron. Optoelectron. '97 Conf.*, Incline Village, NV, 1997.
 - [66] K. Kurishima, H. Nakajima, Y. Fukai, Y. Matsuoka, and T. Ishibashi, "Electron velocity overshoot effect in collector depletion layers of InP/InGaAs heterojunction bipolar transistors," *Jpn. J. Appl. Phys.*, vol. 31, pp. L768–L770, 1992.
 - [67] Y. Muramoto, K. Kato, M. Mitsuhashi, O. Nakajima, Y. Matsuoka, N. Shimizu, and T. Ishibashi, "High-output-voltage, high speed, high efficiency uni-traveling-carrier waveguide photodiode," *Electron. Lett.*, vol. 34, pp. 122–123, 1998.
 - [68] T. Nagatsuma, M. Yaita, M. Shinagawa, K. Kato, K. Iwatsuki, and K. Suzuki, "Electro-optic characterization of ultrafast photodetectors using adiabatically compressed soliton pulses," *Electron. Lett.*, vol. 30, pp. 814–815, 1994.
 - [69] K. Wakita, I. Kotaka, S. Matsumoto, R. Iga, S. Kondo, and Y. Noguchi, "Very-high-allowability of incidental optical power for polarization-insensitive InGaAs/InAlAs multiple quantum well modulators buried in semi-insulating InP," *Jpn. J. Appl. Phys.*, vol. 37, pp. 1432–1435, 1998.
 - [70] M. Yuda, K. Kato, R. Iga, and M. Mitsuhashi, "High-input-power-allowable uni-traveling-carrier waveguide photodiode with semi-insulating-InP-buried structure," *Electron. Lett.*, submitted for publication.
 - [71] K. J. Williams, R. D. Esman, and M. Dagenais, "Effects of high space-charge fields on the response of microwave photodetectors," *IEEE Photon. Technol. Lett.*, vol. 6, pp. 639–641, May 1994.
 - [72] Y. Miyamoto, M. Yoneyama, K. Kato, and H. Tsunetsugu, "40 Gbit/s optical receiver module using a flip-chip bonding technique for device interconnection," *Electron. Lett.*, vol. 34, pp. 493–494, 1998.
 - [73] T. Otsuji, K. Kato, T. Nagatsuma, and M. Yoneyama, "10 to 72 Gb/s RZ pulse pattern generation and its application to on-wafer large-signal characterization for ultrahigh-speed electronic devices," in *LEOS Annu. Meeting*, 1994.
 - [74] Y. Yamada, A. Takagi, I. Ogawa, and M. Kawachi, "Silica-based optical waveguide on terraced silicon substrate as hybrid integration platform," *Electron. Lett.*, vol. 29, pp. 444–446, 1993.
 - [75] E. Sano, M. Yoneyama, S. Yamahata, and Y. Matsuoka, "23 GHz bandwidth monolithic photoreceiver compatible with InP/InGaAs double-heterojunction bipolar transistor fabrication process," *Electron. Lett.*, vol. 30, pp. 2064–2065, 1994.
 - [76] A. L. Gutierrez-Aitken, K. Yang, X. Zhang, G. I. Haddad, and P. Bhattacharya, "16 GHz bandwidth InAlAs/InGaAs monolithically integrated pin-HBT photoreceiver," in *ECOC'95*, 1995, pp. 661–664.
 - [77] U. Westergren, B. Willén, and H. Asonen, "20 GHz bandwidth monolithic optoelectronic receiver based on SSBME-grown InP HBT technology," *Electron. Lett.*, vol. 32, pp. 1719–1720, 1996.
 - [78] B. U. H. Klepser, J. Spicher, C. Bergamaschi, W. Patrick, and W. Bächtold, "High speed, monolithically integrated pin-HEMT photoreceiver fabricated on InP with a tunable bandwidth up to 22 GHz using a novel circuit design," in *Int. Conf. Indium Phosphide Related Materials'96*, 1996, pp. 443–446.
 - [79] P. Fay, W. Wohlmut, C. Caneau, and I. Adesida, "18.5-GHz bandwidth monolithic MSM/MODFET photoreceiver for 1.55- μm wavelength communication systems," *IEEE Photon. Technol. Lett.*, vol. 8, pp. 679–681, May 1996.
 - [80] S. Kimura, Y. Imai, Y. Umeda, and T. Enoki, "0–90 GHz InAlAs/InGaAs/InP HEMT distributed baseband amplifier IC," *Electron. Lett.*, vol. 31, pp. 1430–1431, 1995.
 - [81] A. Umbach, S. V. Waasen, U. Auer, H. G. Bach, R. M. Bartenburg, V. Breuer, W. Ebert, G. Janssen, G. G. Mekonnen, W. Passenberg, W. Schlaak, C. Schramm, A. Seeger, G. J. Tegude, and G. Unterbörsh, "Monolithic pin-HEMT 1.55 μm photoreceiver on InP with 27 GHz bandwidth," *Electron. Lett.*, vol. 32, pp. 2142–2143, 1996.
 - [82] Y. Muramoto, K. Takahata, H. Fukano, K. Kato, A. Kozen, O. Nakajima, and Y. Matsuoka, "46.5 GHz bandwidth monolithic receiver OEIC consisting of a waveguide P-I-N photodiode and a distributed amplifier," in *ECOC'97*, vol. 5, 1997, pp. 37–40.
 - [83] H. G. Bach, W. Schlaak, G. G. Mekonnen, R. Steingruber, A. Seeger, T. Engel, W. Passenberg, A. Umbach, C. Schramm, and G. Unterbörsh, "50-Gbit/s InP-based photoreceiver OEIC with gain flattened transfer characteristics," in *ECOC'98*, vol. 1, 1998, pp. 55–56.
 - [84] K. Takahata, Y. Miyamoto, Y. Muramoto, H. Fukano, and Y. Matsuoka, "50-Gbit/s operation of monolithic WGPDM/HEMT receiver OEIC module," in *ECOC'98*, vol. 3, 1998, pp. 67–68.



Kazutoshi Kato (A'91–M'93) was born in Yokohama, Japan, on January 29, 1961. He received the B.S and M.S. degrees in physics and the Ph.D. degree from Waseda University, Tokyo, Japan, in 1985, 1987, and 1993, respectively.

Since 1987, he has been with NTT Opto-Electronics Laboratories, Kanagawa, Japan, where he had been engaged in research on receiver OEIC's and high-speed p-i-n PD's. From 1994 to 1995, he was on leave from NTT at France Telecom CNET Bagneux Laboratory, France, as a Visiting

Researcher working on MSM PD's. He is currently a Senior Research Engineer at the NTT Photonics Laboratories, Atsugi, Kanagawa, Japan, where he is currently researching future broad-band photonic networks, as well as photoreceivers for wide-band transmissions, microwave applications, and optical access networks.

Dr. Kato is a member of the Institute of Electronics, Information and Communication Engineers (IEICE), Japan, the Japan Society of Applied Physics, and the IEEE Lasers and Electro-Optics Society (LEOS).